Materials Today Bio 27 (2024) 101158

Contents lists available at ScienceDirect

Materials Today Bio

journal homepage: www.journals.elsevier.com/materials-today-bio

Silk fibroin microgrooved zirconia surfaces improve connective tissue sealing through mediating glycolysis of fibroblasts

Yinuo Yan [a,b,1], Qiqian Yan [a,b,1], Kexin Cai [a,b,1], Zhihan Wang [a,b], Qiulan Li [a,b], Ke Zha [a,b,**], Yutao Jian [a,b,***], Xiaoshi Jia [a,b,*]

[a] Guanghua School of Stomatology, Hospital of Stomatology, Sun Yat-sen University, 56 Lingyuan West Road, Guangzhou, Guangdong, 510055, China
[b] Guangdong Provincial Key Laboratory of Stomatology, Guangzhou, China

ARTICLE INFO

Keywords:
Connective tissue sealing
Zirconia abutments
Microgrooves
Inkjet printing
Glycolysis

ABSTRACT

The use of zirconia has significantly enhanced the aesthetic outcomes of implant restorations. However, peri-implantitis remains a challenge to long-term functionality of implants. Unlike the perpendicularly arranged collagen fibers in periodontal tissue, those in peri-implant tissue lie parallel to the abutment surface and contain fewer fibroblasts, making them more prone to inflammation. Studies have shown that microgroove structures on implant abutments could improve surrounding soft tissue structure. However, creating precise microgrooves on zirconia without compromising its mechanical integrity is technically challenging. In this study, we applied inkjet printing, an additive manufacturing technique, to create stable silk fibroin microgroove (SFMG) coatings of various dimensions on zirconia substrates. SFMG significantly improved the hydrophilicity of zirconia and showed good physical and chemical stability. The SFMG with 90 μm interval and 10 μm depth was optimal in promoting the proliferation, alignment, and extracellular matrix production of human gingival fibroblasts (HGFs). Moreover, the *in vitro* results revealed that SFMG stimulated key glycolytic enzyme gene expression in HGFs via the PI3K-AKT-mTOR pathway. Additionally, the *in vivo* results of histological staining of peri-abutments soft tissue showed that SFMG promoted the vertical alignment of collagen fibers relative to the abutment surface, improving connective tissue sealing around the zirconia abutment. Our results indicated that SFMG on zirconia can enhance HGF proliferation, migration and collagen synthesis by regulating glycolysis though PI3K-AKT-mTor pathway, thereby improving connective tissue sealing.

1. Introduction

Implant-supported restorations are widely favored in clinical settings for their benefits, including the preservation of adjacent teeth and enhanced masticatory efficiency [1]. Nevertheless, implant failure rates caused by peri-implant inflammation was as high as 20 % [2–4], without the influence of implant or abutments materials [5]. The genesis of peri-implantitis, similar to periodontitis, is primarily due to bacterial biofilm formation and subsequent bacterial invasion [6]. However, peri-implantitis progresses more swiftly and causes more extensive tissue damage due to the differences in tissue architecture between natural periodontal tissues and peri-implant tissues [7]. Specifically, peri-implant connective tissue lacks the perforating fibers in natural dental connective tissue, weakening its resistance to the apical migration of epithelial cells, a precursor to peri-implantitis [8]. Additionally, the connective tissue near abutments contains lower concentration of type I and type III collagen, an elevated level of type V collagen, and reduced fibroblasts, which leads to a marked decrease in tissue repair capabilities after inflammation [9]. Given these challenges, it is crucial to develop strategies that bolster the structure and composition of peri-implant connective tissue. Improving the integration and sealing properties of soft tissues around implant abutments and restorations is essential for mitigating the risks associated with peri-implant inflammation.

In recent years, the use of zirconia abutments in clinical practice had significantly increased. Zirconia has mechanical properties comparable

* Corresponding author. Guanghua School of Stomatology, Sun Yat-sen University, Guangzhou, Guangdong, 510055, China.
** Corresponding author. Department of Prosthodontics, Sun Yat-sen University, Guangzhou, Guangdong, 510055, China.
*** Corresponding author. Guanghua School of Stomatology, Sun Yat-sen University, Guangzhou, Guangdong, 510055, China.
E-mail addresses: zhaoke@mail.sysu.edu.cn (K. Zhao), jianyt@mail.sysu.edu.cn (Y. Jian), jiaxsh3@mail.sysu.edu.cn (X. Jia).
[1] These authors contributed equally.

https://doi.org/10.1016/j.mtbio.2024.101158
Received 1 April 2024; Received in revised form 12 July 2024; Accepted 12 July 2024
Available online 14 July 2024

to titanium, fully supporting the masticatory function of restorations in the mouth [10]; Compared to traditional titanium abutments, zirconia abutments have superior aesthetic performance, significantly reducing the risk of gingival translucency in anterior dental implants [11]; Zirconia abutments are also known for their bacterial resistance, with a biologically inert surface that is less prone to bacterial attachment compared to titanium, reducing the risk of infection in the surrounding tissues [12]. However, the biologically inert surface of zirconia also affects its integration with the surrounding soft tissues. Studies have found that compared to titanium abutments, the sealing ability of connective tissue around zirconia abutments was relatively weaker, which might adversely affect the long-term stability of both soft and hard tissues around the implant [13,14].

The extracellular substrate topography and the geometric patterns of the substrate surfaces influence cellular functions, known as contact guidance [15,16]. Nanotube and microgroove structures on zirconia and titanium surfaces have been found to promote the proliferation of gingival fibroblasts [17]. Compared to the surfaces treated with non-patterned techniques such as acid etching and sandblasting, the surfaces with groove structure were more conducive to enhancing the bioactivity of the abutment [18]. Microgroove structures on titanium abutment surfaces have been shown to encourage the development of vertically oriented fibers [19] and to deter the apical migration of epithelial cells along the abutment [20]. However, existing methods for creating microgrooves on abutment surfaces are predominantly subtractive, significantly reducing the mechanical integrity of zirconia abutments [21], thus constraining the use of grooved structures on zirconia and related research. Moreover, the effectiveness of contact guidance is contingent upon the size of the microgrooves, and there is currently no agreed-upon optimal dimension for maximizing connective tissue integration [17].

Inkjet printing emerged as a versatile patterning method that employs voltage-driven mechanisms to deposit coating materials without compromising the structural and mechanical integrity of the underlying material [22]. This technology facilitated the exact and programmable creation of patterned surfaces, thereby minimizing material waste [23]. The selection of bio-ink is vital for ensuring the biological effectiveness of the coated surface, with recent studies exploring the use of bioactive substances like platelet lysates and fibrinogen to enhance tissue compatibility of implant [24–28]. Despite their benefits, these materials often presented challenges related to immunogenicity and required extensive separation and purification processes, elevating costs and increasing the risk of infection [29]. Silk fibroin (SF) is a natural bioprotein derived from silkworm silk, composed of a heavy chain of 350 kDa and a light chain of 25 kDa, connected by disulfide bonds [30]. Due to the industrial scalability, excellent biocompatibility, and robust mechanical attributes, SF has been successfully applied in the development of biomaterials for bones [31] and blood vessels [29] regeneration. Besides, SF solution could promote the migration and proliferation of fibroblasts (key effector cells in soft tissue healing) [32] and the healing of skin wounds [30]. Furthermore, the rheological characteristics of SF solutions make them well-suited for use as bio-inks [33].

Recently, cellular metabolism was found may be a key pathway through which surface morphology regulated cell behavior [34,35]. Glyco-metabolism is the primary source of cellular energy and one of the most likely metabolic pathways to impact cell behavior [36]. Ball et al. [37] found that changes in titanium roughness could affect osteoblast glucose metabolism, thereby influencing ALP expression. Different substrate hardness could alter the glycolysis process of fibroblasts, thereby regulating their proliferation and synthesis of collagen fibers [38]. These findings collectively suggested that cellular glyco-metabolism plays a crucial role in the regulation of cell behavior in response to surface morphology.

This study aimed to develop silk fibroin microgroove (SFMG) coatings on zirconia substrates utilizing inkjet printing technology, assess the efficacy of SFMG coatings in enhancing connective tissue integration, and investigate the underlying mechanisms. The outcomes of this investigation are expected to contribute new insights and theoretical underpinnings for the advancement of ceramic material surfaces and soft tissue integration with zirconia abutments.

2. Materials and methods

2.1. Preparation of SFMG coatings on zirconia

Commercial zirconia discs (33 mm, 15 mm and 3.5 mm in diameter, 0.8 mm in thickness) (Dachuan Ceramics, China) served as the substrates for our *in vitro* experiments. For the *in vivo* studies, Zirconia abutment (cubes with 1.5 mm edges, Dachuan Ceramics, China) and titanium implants (Gensray CNC, China) (Supplemental materials 1) were employed. These components were securely bonded using Panavia adhesive (Kuraray, Japan). The zirconia materials used in this study were all yttria-stabilized tetragonal zirconia polycrystals, and the titanium metal was commercial-grade five titanium.

Anhydrous sodium carbonate (4.24 g) was dissolved in 2 L ultrapure water at 100 °C to prepare a 0.02 M sodium carbonate solution. Chopped mulberry silkworm cocoons (5 g, Northwest Silkworm Base, China) were added into the boiled sodium carbonate solution for 120 min with stirring to be degummed. After degumming, the solution was removed through a filter, to get the degummed SF, rinsed with ultrapure water 3 times at room temperature. At this stage, the SF appeared as a fibrous clump (Fig. 1a). The agglomerate SF was spread on a clean piece of tin foil and dried in a drying oven at 37 °C overnight (Fig. 1b). The dried SF fibers were added into lithium bromide (LiBr, Xiya Reagent, China) solution (9.3 M) (the volume of LiBr solution required is four times the mass of SF). The solution contained SF fibers was heated in a water bath at 60 °C for 4 h until the SF fibers was completely dissolved. Now the solution became an amber-colored transparent liquid (Fig. 1c). Dialyze the SF solution with a dialysis membrane with a molecular weight cutoff of 14 kDa and ultrapure water, dialysis lasts for 2 days, changing the water 8 times, every 6 h (Fig. 1d). The dialyzed solution was then centrifuged at 4 °C, 8000 rpm for 20 min, the supernatant was centrifuged again under the same conditions to thoroughly remove impurities. The SF solution was stored at 4 °C and used within one month (Fig. 1e).

SF solution (4 %, w/v) was filled into the printing nozzle (5 μm in diameter). Utilizing a super inkjet printer (SIJ-S150, Japan), SFMG parallel lines with certain intervals were constructed on the surface of zirconia according to the design pattern. These intervals, referred to as 'widths' in our study, represented the spacing between SF ridges rather than the widths of the SF ridges themselves. The widths of the microgrooves were set at 30 μm, 60 μm, and 90 μm, while the depths were set at 5 μm or 10 μm (each group is represented by width/depth). These intervals were controlled by adjusting the printing nozzle intervals. Considering that the SF ridges themselves have a certain width (approximately 30 μm), we set the printing nozzle interval to the required interval plus the width of the SF ridges to construct grooves with specific intervals. For instance, to construct grooves with a spacing of 90 μm, we need to set the printing interval to 120 μm, which includes the 90 μm spacing plus the 30 μm width of the SF ridges. The depth of the coating was regulated by the total number of printing passes: 50 cycles for achieving a 5 μm depth and 100 cycles for a 10 μm depth. The printing was executed under a voltage of 600 V, with a speed set at 20 mm/s and an acceleration of 10 mm/s^2. Plain zirconia and SF-coated discs without grooves (thickness: 5 μm) served as the control groups, labeled as Control and SF, respectively (Fig. 1f). After printing, the samples were submerged in anhydrous ethanol for 1 h and left to dry in the drying oven at 37 °C overnight (Fig. 1g).

2.2. Specimen characterization

The rheological properties of the SF solution were evaluated using a rotational rheometer (3790340, HAAKE, Germany). The SF solution's

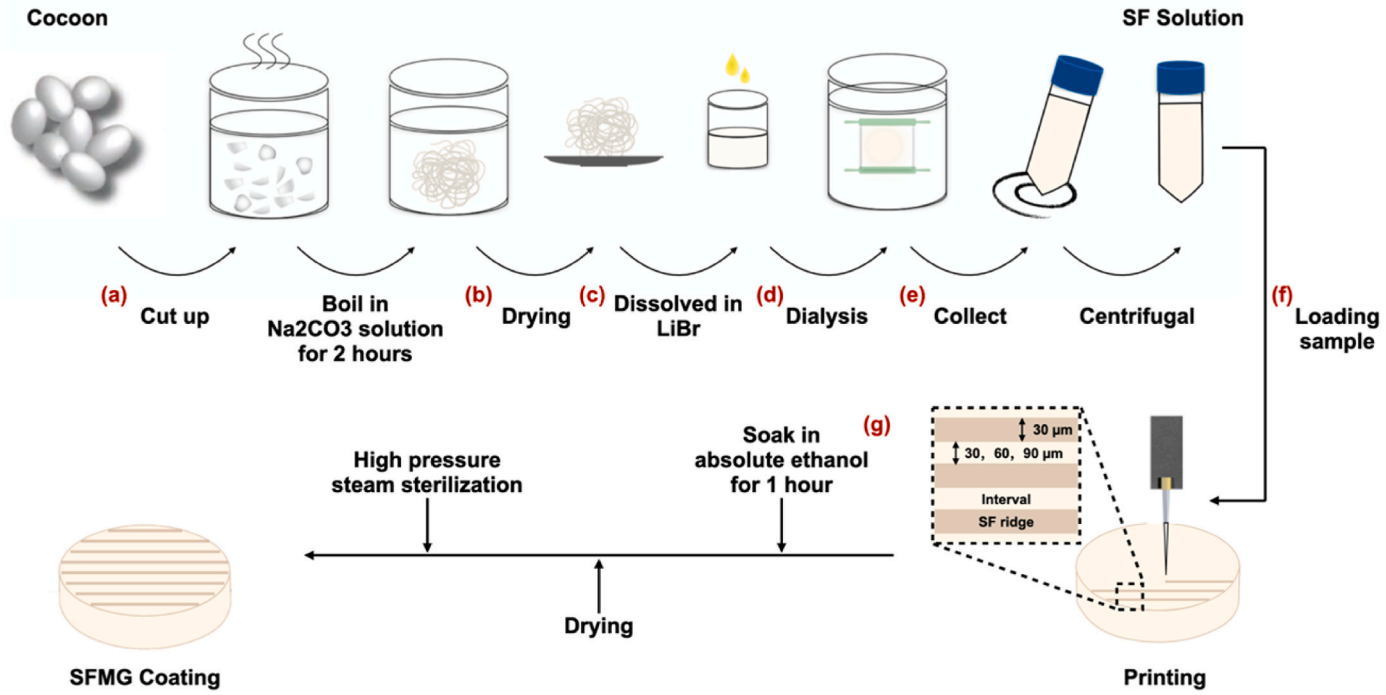

Fig. 1. Process diagram for preparing SFMG.

surface tension and dynamic contact angle with the zirconia surface were determined using an optical surface tension meter (Theta Flow, Attention, Sweden). The size and zeta potential of solutes in the SF solution were measured using the nanoparticle tracking analysis (NTA) (Particle Metrix, Zeta View, Germany). A camera (D750, Canon, Japan) was used to capture the macroscopic images of the SFMG on the zirconia surface. The morphologies of the fabricated SFMG coatings were examined using a polarized light microscope (PLM, SANYO, Japan) and a confocal laser scanning microscope (CLSM, LSM700, ZEISS, Germany). To further assess the thickness of the coating, we analyzed the cross-section (perpendicular to the groove direction) of the coating with a scanning electron microscopy (SEM, Phenom-World, the Netherlands). To assess the stability of the coatings, the samples were submerged in artificial saliva for 28 days, mirroring the time required for soft tissue integration around dental abutments [39]. Changes in the coatings' morphology and chemical composition before and after immersion were analyzed using PLM and fourier-transform infrared spectroscopy (FTIR, Nicolet iS20, Thermo, America).

2.3. In vitro experiment

2.3.1. Cell culture and treatment with inhibitors

Primary HGFs were isolated using an enzymatic digestion method from gingival connective tissues harvested from patients undergoing third molar extractions (Ethical number: KQEC2019-37). HGFs were then cultured in Dulbecco's modified eagle's medium (DMEM, Gibco, America), supplemented with 10 % (v/v) fetal bovine serum (FBS, Gibco, America) and 1 % penicillin-streptomycin (P/S, Beyotime, China). The cell cultures were maintained in T25 culture flasks at 37 °C in a humidified incubator with 5 % CO_2. Subculturing was performed once the cell confluence reached approximately 80 %–90 % within the flasks. For the experiments, cells between passages 3 to 6 were employed.

To suppress glycolytic activity in HGFs, the cells were treated with a glycolysis inhibitor, 2-Deoxy-D-glucose (2-DG, HY-13996, medchemexpress (MCE), 15 mM/mL), for 24 h. Cells that did not receive the 2-DG treatment served as the control group.

Furthermore, HGFs were exposed to 2-Morpholino-8-benzylchromone (LY294002, HY-10108, MCE, 10 μM/mL), a PI3K inhibitor, for 24 h to block the PI3K-AKT pathway. Cells untreated with LY294002 were utilized as the control for the current experiments.

2.3.2. The cell cytoskeleton of HGFs cultured on SFMG coatings

HGFs cultured on different zirconia discs within 24-well cell culture plates for 24 h were gently washed three times with phosphate-buffered saline (PBS, Beyotime, China) and subsequently fixed with 4 % paraformaldehyde (PFA, Beyotime, China) for 20 min. Following fixation, the cells were permeabilized using a 0.2 % Triton™ X-100 in PBS solution (Biosharp, China) for 5 min. After permeabilization, the cells were stained with fluorescein isothiocyanate (FITC)-labeled phalloidin (1:50, Beyotime, China) to visualize the actin filaments and counterstained with 4',6-diamidino-2-phenylindole (DAPI, Beyotime, China) for nuclear visualization. Representative fluorescence images were captured utilizing a CLSM (LSM980, ZEISS, Germany).

2.3.3. Cell proliferation assay

HGFs were seeded onto zirconia samples within 96-well cell culture plates. At a density of 1×10^4 cells per well and were cultured for 24 h. Following this, the proliferation of HGFs was assessed using an EdU assay kit (KGA9602-100, KeyGEN Biotech, China). The cells were incubated with a 10 μM EdU solution under constant temperature conditions, fixed with 4 % PFA, and neutralized with glycine (2 mg/mL). Subsequently, cells were permeabilized using a 0.2 % Triton™ X-100 in PBS solution for 5 min. The Click-iT reaction was applied to label EdU-positive cells, while DAPI staining was utilized to label all cells. The proportion of EdU-positive cells relative to the total cell count was determined by capturing images with a CLSM (Axio observer Z1, ZEISS, Germany).

CCK-8 (CK04, Dojindo, Japan) was utilized to evaluate the proliferation of HGFs cultured on various zirconia discs. The cells were plated at a density of 5×10^3 cells per well on zirconia disks in 96-well cell culture plates. At 1, 3, and 7 days post-seeding, the cells were gently washed three times with PBS. Subsequently, each well received 100 μL of fresh DMEM (without FBS) containing 10 μL of CCK-8 reagent. The cells were then incubated at 37 °C for an additional 2 h. Afterwards, 100 μL of the medium from each well was transferred to a new plate to measure the

optical density at 450 nm using a Microplate Reader (800 TS, BioTek, America).

The group exhibiting the most significant effect in promoting cell proliferation was selected for further experimentation and denoted as the SFMG group.

2.3.4. Quantitative real-time polymerase chain reaction (qRT-PCR) analysis

HGFs were cultured on zirconia discs placed in 6-well cell culture plates, with an initial seeding density of 2×10^5 cells per well. For the analysis of collagen type I (COL1A1) and collagen type III (COL3A1) mRNA expression, cells were incubated for 7 days. In contrast, for the assessment of other mRNA types, a 24-h culture period was applied. This study focused on evaluating the cellular glycolytic capacity by measuring mRNA levels of key enzymes: hexokinase 2 (HK2), phosphoglycerate kinase 1 (PGK1), fructose-2,6-bisphosphatase 3 (PFKFB3), pyruvate kinase M2 (PKM2), and lactate dehydrogenase A (LDHA). Additionally, the cellular oxidative phosphorylation capacity was assessed by examining the mRNA expression of pyruvate dehydrogenase E1 component subunit alpha (PDHA1), dihydrolipoamide dehydrogenase (DLD), dihydrolipoamide S-acetyltransferase (DLAT), isocitrate dehydrogenase 1 (IDH1), and citrate synthase (CS). Following the specified culture periods, total RNA was extracted using an RNA rapid extraction kit (RN001, Yishan, China). Each well was treated with 500 μL of lysis buffer, followed by complete lysis and subsequent neutralization with an equal volume of anhydrous ethanol. The mixtures were then subjected to high-speed centrifugation to eliminate impurities. The purified RNA was resuspended in an elution buffer, and its concentration was determined using a NanoDrop 2000 spectrophotometer (Thermo Scientific, America). Complementary DNA (cDNA) synthesis was performed using the PrimeScript™ RT Reagent Kit (RR036A, TaKaRa, Japan). qRT-PCR was conducted using Hieff® qPCR SYBR Green Master Mix (No Rox) (Yeasen Biotechnology, China), with the prepared cDNA serving as the template. The cycle threshold (CT) values obtained were analyzed, employing glyceraldehyde-3-phosphate dehydrogenase (GAPDH) as the internal control for normalization purposes. Primer sequences for the target genes are listed in Table 1.

Table 1
The primer sequences for the target genes.

Genes	Primers Sequences	
FN	Forward	CGGTGGCTGTCAGTCAAAG
	Reverse	AAACCTCGGCTTCCTCCATAA
COL1A1	Forward	GAGGGCCAAGACGAAGACATC
	Reverse	CAGATCACGTCATCGCACAAC
COL3A1	Forward	GGAGCTGGCTACTTCTCGC
	Reverse	GGGAACATCCTCCTTCAACAG
PDHA1	Forward	TGGTAGCATCCCGTAATTTTGC
	Reverse	ATTCGGCGTACAGTCTGCATC
DLAT	Forward	CGGAACTCCACGAGTGACC
	Reverse	CCCCGCCATACCCTGTAGT
DLD	Forward	CTCATGGCCTACAGGGACTTT
	Reverse	GCATGTTCCACCAAGTGTTTCAT
CS	Forward	TGCTTCCTCCACGAATTTGAAA
	Reverse	CCACCATACATCATGTCCACAG
IDH1	Forward	TGTGGTAGAGATGCAAGGAGA
	Reverse	TTGGTGACTTGGTCGTTGGTG
PI3K	Forward	GGAGCTGGCTACTTCTCGC
	Reverse	GGGAACATCCTCCTTCAACAG
HK2	Forward	GAGCCACCACTCACCCTACT
	Reverse	CCAGGCATTCGGCAATGTG
PKM2	Forward	ATGTCGAAGCCCCATAGTGAA
	Reverse	TGGGTGGTGAATCAATGTCCA
PGK1	Forward	TGGACGTTAAAGGGAAGCGG
	Reverse	GCTCATAAGGACTACCGACTTGG
LDHA	Forward	ATGGCAACTCTAAAGGATCAGC
	Reverse	CCAACCCCAACAACTGTAATCT
PFKFB3	Forward	TTGGCGTCCCCACAAAAGT
	Reverse	AGTTGTAGGAGCTGTACTGCTT
GAPDH	Forward	TTGCAGTGGCAAAGTGGAGA
	Reverse	GATGGGCTTCCCGTTGATGA

2.3.5. Western blot analysis

HGFs were seeded onto zirconia discs placed in 6-well cell culture plates at a density of 2×10^5 cells per well. For the analysis of fibronectin (FN) and proteins related to the PI3K-AKT pathway, cells were cultured for 24 h. For collagen-related proteins, the culture period was extended to 7 days. The cells were lysed using RIPA buffer containing 1 % protease and phosphatase inhibitors, followed by centrifugation at 15,000 g for 20 min at 4 °C. Protein concentrations were determined using the Bicinchoninic Acid (BCA) Protein Assay Kit (XL357479, Thermo Scientific, America). The cell lysates were then mixed with sodium dodecyl sulfate (SDS) sample loading buffer (#20315ES05; Yeasen Biotechnology, China) and heated for 10 min at 95 °C to denature the proteins. These denatured proteins were loaded into pre-made gels (M00657, GenScript, America) and subjected to electrophoresis, followed by transfer to PVDF membranes. The membranes were blocked with 5 % bovine serum albumin (BSA, Beyotime, China) for 1 h at room temperature. After three washes with PBS, the membranes were incubated overnight at 4 °C with primary antibodies targeting FN (ab268020, Abcam, UK), COL1A1 (BA0325, Boster, China), COL3A1 (68320-1-Ig, Proteintech, China), GAPDH (60004-1-Ig, Proteintech, China), PI3K (4257T, Cell Signaling Technology (CST), America), phospho-AKT (P-AKT, 4060T, CST, America), and phospho-mTOR (P-mTOR, 66888-1-Ig, Proteintech, China). Following another set of three PBS washes, the membranes were incubated with respective secondary antibodies (Jackson, America) at room temperature for 1 h. Protein bands were visualized using an electrochemiluminescence plus reagent (Bio-Rad, ChemiDoc, America), and images were captured for analysis. For the assessment of phosphorylated proteins, after the initial exposure, membranes were washed three times with Stripping Buffer (Beyotime, China), re-sealed, and then re-incubated with primary antibodies targeting AKT (4691S, CST, America) and mTOR (66888-1-Ig, Proteintech, China), followed by incubation with respective secondary antibodies and re-exposure for imaging.

2.3.6. Cell migration

Transwell assay was utilized to assess the impact of SFMG on the migration of HGFs. In short, HGFs were plated in the upper chambers of a 24-well Transwell plate (Corning, with a pore size of 8 μm) at a density of 2×10^4 cells per well. Subsequently, 600 μL of DMEM, containing supernatants collected from various groups in which HGFs had been previously cultured for 24 h, was introduced into the lower chambers. After a culture period of 24 h, non-migrated cells on the upper surfaces of the upper chamber filters were gently removed using a cotton swab. The filters' lower surfaces were then fixed with 4 % PFA and stained with 0.1 % crystal violet for 10 min. Migration was quantified by examining five randomly chosen fields per filter under a microscope (CKX53, OLYMPUS, Japan).

2.3.7. RNA sequencing and data analysis

HGFs were cultured on zirconia discs in 6-well cell culture plates at a density of 2×10^5 cells per well for 24 h. The cells were lysed using Trizol reagent (Beyotime, China), and the resultant lysates were submitted to Nanjing Persomics Genetech Company Limited for mRNA isolation, construction of Illumina sequencing libraries, synthesis of double-stranded cDNA, bioinformatics analysis, and high-throughput sequencing. Each experimental group was represented by three biological replicates. Differentially expressed genes (DEGs) were defined based on a log2-fold change (FC) $> |1|$ and a p-value <0.01. To understand the biological implications of these DEGs, enrichment analysis was conducted utilizing the Kyoto Encyclopedia of Genes and Genomes (KEGG) database to identify significant signaling pathways impacted by the DEGs (threshold: p-value <0.05).

2.4. In vivo experiment

2.4.1. Implant surgical and histological examination

Animal experiments were conducted following approval from the Institutional Animal Care and Use Committee (IACUC) of Sun Yat-sen University (approval no. SYSU-IACUC-2022-001406) and in accordance with the ethical standards established by the Animal Ethical and Welfare Committee of Sun Yat-sen University. Twenty-four male Wistar rats (six weeks old and weighing between 120 and 130 g) were randomly allocated into three groups and maintained according to the animal care guidelines of Sun Yat-sen University. Anesthesia was induced using 5 % pentobarbital sodium (0.3 mL per 100 g body weight). The experimental procedure began with the extraction of the bilateral upper first molars, which was accomplished using minimally invasive extraction forceps and vascular clamps to minimize damage to the soft and hard tissues. 4 weeks after the extraction, once the hard and soft tissues at the extraction sites had healed, the implant surgery was performed as the procedures described before [40]. A full thickness mucoperiosteal flap was carefully elevated to expose the underlying bone at the implant site. Subsequently, custom-made twist drills (diameters 1 mm, 1.5 mm, and 2.0 mm) were used for gradual drilling, during which 50 mL syringes continuously dripped physiological saline to locally cool the area. Finally, a screwdriver was used to place the micro-implants with a zirconia base into these prepared sites. After an additional 4-week healing period, euthanasia was performed on the rats through overdose anesthesia, and the small implants along with the surrounding soft tissues were simultaneously excised. The collected samples were immediately fixed in 4 % PFA (Beyotime, China), then immersed in a decalcifying solution composed of 5 % ethylenediaminetetraacetic acid (EDTA, Beyotime, China) and 4 % sucrose (diluted in 0.01 M PBS (Beyotime, China)), and stored at 4 °C for 4 days for decalcification. The procedure of obtaining soft tissue samples was performed as described before [40]. After decalcification, the buccal gingival tissues were peeled off from the surface of the implants. Because the peeling action may damage the interface between the gingiva and the implants, this part of the tissue was not used. The remaining tissues were gently stirred at 4 °C in the same decalcifying solution for one day, until the implants and soft tissues naturally separated, then the mandibular side soft tissues were taken for further analysis.

After the samples were embedded in paraffin, serial sections with a thickness of 5 μm were prepared using a microtome (RM2255, Leica Biosystems, Germany), followed by Masson's trichrome staining. The stained sections were then digitally imaged using a slide scanning system (Aperio AT2, Leica Biosystems, Germany) for detailed examination and analysis.

2.4.2. Immunofluorescence staining

The sections were subjected to antigen retrieval by boiling in antigen repair solution (G1203, Servicebio, China) for 15 min. Following this, they were rinsed with PBS and blocked with bovine serum albumin (BSA, GC305010, Servicebio, China) for 20 min to prevent non-specific binding. The sections were then incubated with a primary antibody against FN (GB114491, Servicebio, China) overnight at 4 °C. After washing with PBS, they were incubated with a secondary antibody (111-585003, Jackson, America) at 37 °C for 1.5 h. Subsequent to another PBS rinse, the cell nuclei were counterstained with DAPI (1:100, Beyotime, China). Following the staining process, the sections were dehydrated, cleared with xylene (Sigma-Aldrich, America) for 1 min, air-dried, and finally mounted using neutral resin. Images of the sections were acquired using a CLSM (FV3000, OLYMPUS, Japan) for detailed analysis.

2.4.3. HRP penetration experiment

Four weeks post-implantation, rats underwent anesthesia following the protocol outlined in section 2.3.1. Cotton threads saturated with a 50 mg/mL horseradish peroxidase (HRP)-infused saline solution were gently positioned around the gingival margins of the implants, ensuring no mechanical stress was applied. An additional saline solution containing HRP was applied to the cotton every 10 min over 1 h. Subsequent to the treatment, the samples were harvested, embedded, and sectioned as detailed in section 2.3.1. The obtained sections were then processed using a DAB staining kit (LM80010C, LMAI Bio, China). The extent of HRP penetration within the tissue sections was assessed using a digital slide scanning system (Aperio AT2, Leica, Germany).

2.5. Statistical analysis

All statistical analyses were performed using GraphPad Prism 9.0 (GraphPad Software, USA). All experiments were conducted in triplicate, and data were presented as mean ± standard deviation (SD). One-way ANOVA was used to assess differences between group means, with Levene's test initially testing for homogeneity of variances. In cases where Levene's test indicated variance inequality, the Brown-Forsythe test was employed. When variances were equal, Tukey's Honestly Significant Difference (HSD) test was used for post hoc comparisons; if variances were unequal, the Games-Howell test was applied. Statistical significance was set at $p < 0.05$.

3. Results

3.1. Printing performance of SF solution

The SF solution demonstrated shear-thinning properties, with its viscosity measured at 3 mPa s in the second Newtonian plateau, indicating its suitability for printing (Fig. 2A). Additionally, the surface tension of the SF solution was recorded at 44.41 ± 0.05 mN/m (Fig. 2B), which falls within the optimal range for inkjet printing. Dynamic contact angle assessments between the SF solution and the zirconia substrate revealed a moderate level of ink-substrate interaction, showcasing the potential for adequate adhesion and spreading of the SF solution on the zirconia surface (Fig. 2C a, b). The NTA results indicated that the particle size of solutes in the SF solution was 128.3 ± 58.2 nm, and the zeta potential was −35.41 ± 1.44 mV, which were consistent with the basic characteristics of proteins and meet the requirements for piezoelectric inkjet printing (Fig. 2D and E).

3.2. Morphology of SFMG-coated zirconia surface

Images of camera and PLM confirmed the successful formation of consistent and uniform SFMG coatings on the zirconia surfaces using an inkjet printing method (Fig. 3A–C). Furthermore, three-dimensional reconstructions obtained from CLSM and the images of SEM displayed that the coatings achieved depths of 5 and 10 μm and widths of 30, 60, and 90 μm, respectively (Fig. 3B–D).

FTIR and PLM analyses were performed to assess the degradation of the SFMG coatings. FTIR spectra maintained the characteristic peaks of SF within the coatings (C═O at 1620 cm^{-1}, N–H at 1515 cm^{-1}, and C–N at 1235 cm^{-1}), but the diminished peak intensities suggested partial degradation of the SFMG (Fig. 4A). However, the PLM images did not show a significant difference in the morphology of the SFMG coatings (Fig. 4B), suggesting that the observed chemical changes did not substantially alter the overall structural integrity visible under PLM.

3.3. SFMG guided the arrangement of HGFs

CLSM results revealed that HGFs neatly aligned along the microgrooves, with their long axis parallel to the direction of the grooves in the 60/5, 60/10, 90/5, and 90/10 groups. Conversely, HGFs in the control and SF groups displayed a random orientation. The 30/5 and 30/10 groups showed a mixture of cells aligned with the grooves and cells oriented randomly. Additionally, it was observed that cells covered the entire surface area of the specimens in the groups where the groove width was 30 μm. In contrast, for grooves 60 μm and 90 μm in width,

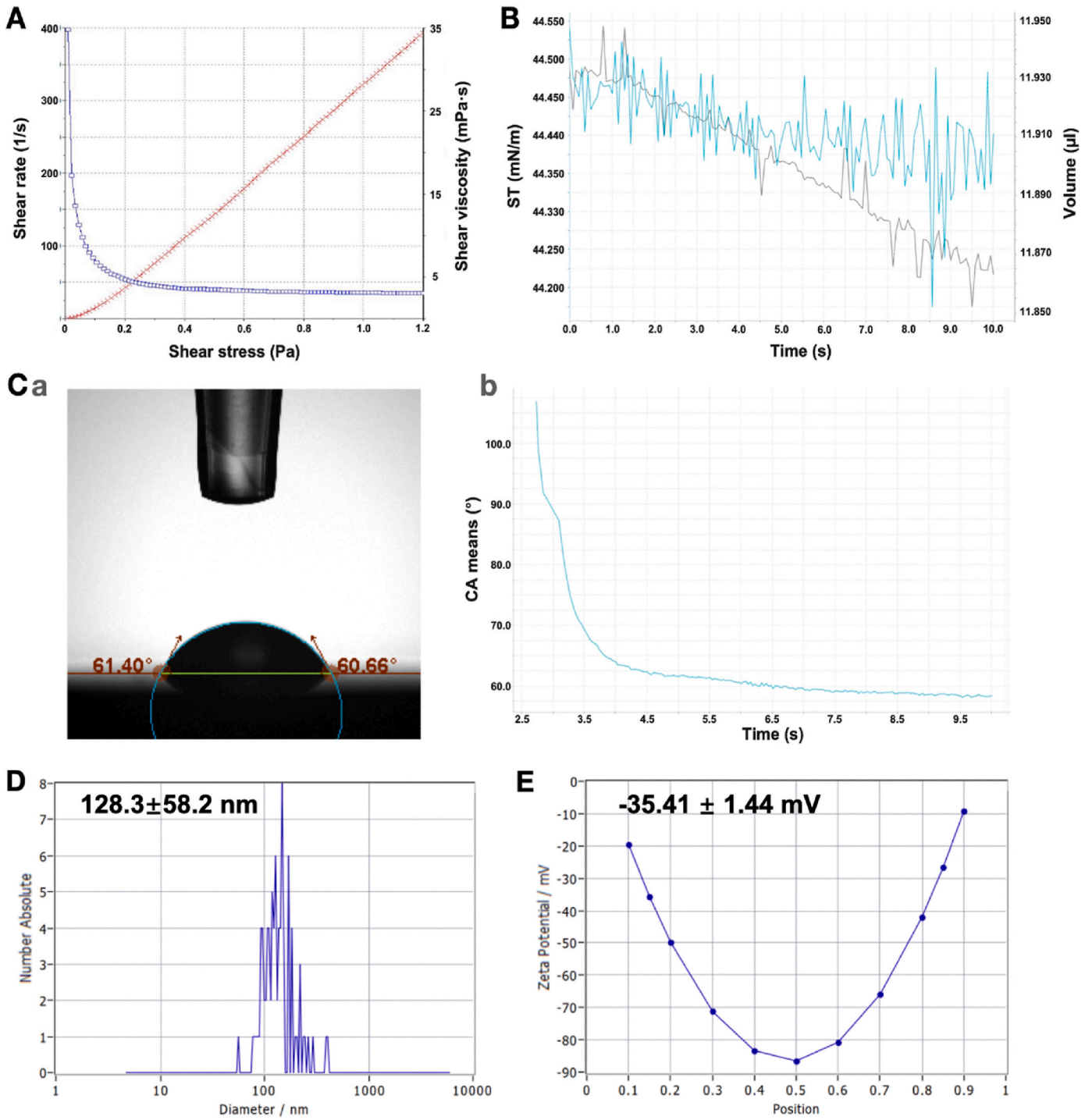

Fig. 2. Physicochemical characterization of SF solution. (A) Dynamic viscosity of SF solution. (B) Surface tension of SF solution. (C) Dynamic contact angle between SF solution and zirconia surface. (D) The presented particle distributions of solute molecule in SF solution by NTA. (E) The presented zeta potential distributions of solute molecule in SF solution by NTA.

cells exhibited a spindle-like morphology and predominantly populated the bottom of the grooves (Fig. 5).

3.4. SFMG promoted the proliferation of HGFs

The EdU incorporation results demonstrated that the percentage of proliferating HGFs was higher in all SFMG groups, with the exception of the 60/10 group, compared to the control group. Notably, the 90/10 group exhibited the highest proliferation rate among the tested groups (Fig. 6A a, b).

Furthermore, the CCK-8 assays indicated that all SFMG coatings enhanced the proliferation of HGFs more effectively than the uncoated control group after 3 and 7 days of culture. Specifically, the 90/10 SFMG coating showed the most pronounced effect on cell proliferation (Fig. 6B). Consequently, this particular SFMG coating size was chosen for further investigation and referred to as the SFMG group in subsequent experiments.

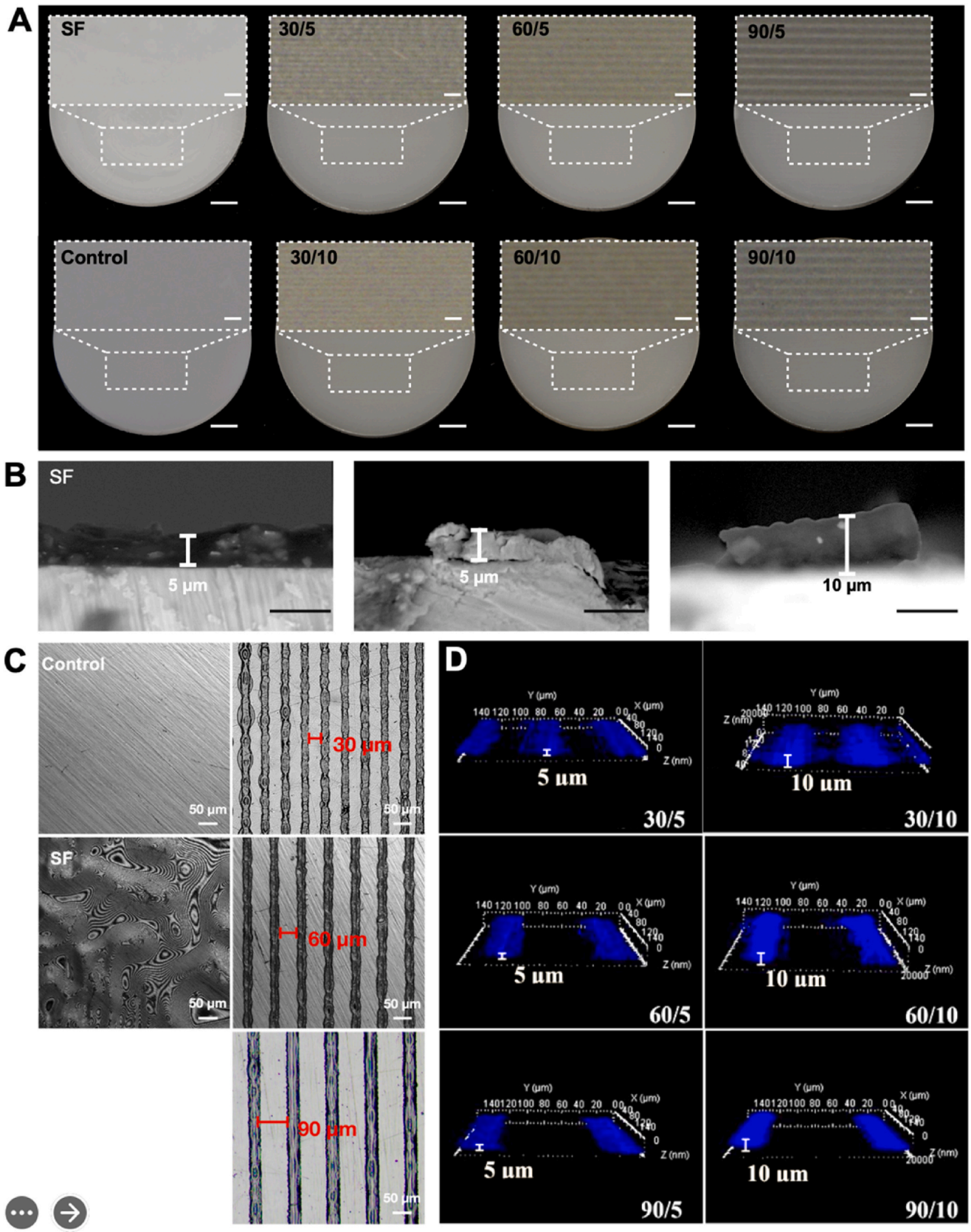

Fig. 3. Morphology characterization of SFMG coatings on zirconia. (A) Macroscopic (Scale bar = 3 mm) and locally magnified images of SFMG (Scale bar = 200 μm) on zirconia surface (B) Cross-sectional SEM Image of SFMG (Scale bar = 10 μm). (C) The morphology of zirconia surface without SF (control group) and with SF uniformly sprayed (SF group) and SFMG coatings of different widths (PLM, Scale bar = 50 μm). (D) Three-dimensional reconstruction of SFMG coatings with different combinations of widths and depths (CLSM, 100 ×).

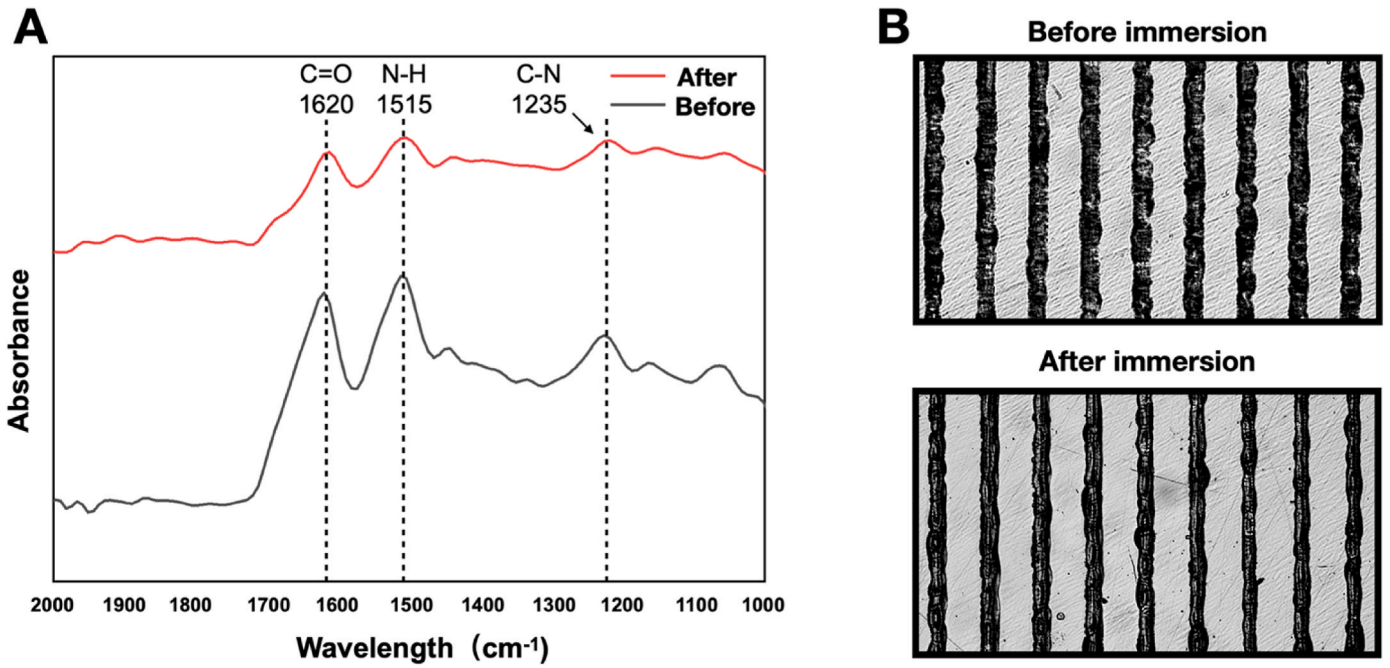

Fig. 4. Stability of SFMG coatings on zirconia surface. (A) FTIR spectrum of SFMG coatings before and after immersion in artificial saliva. The y-axis is only applicable to the lowest curve, and for clarity, the remaining curve moved vertically. The dashed line represents the main peak. (B) Surface morphology of SFMG coatings before and after immersion in artificial saliva (PLM, Scale bar = 100 μm).

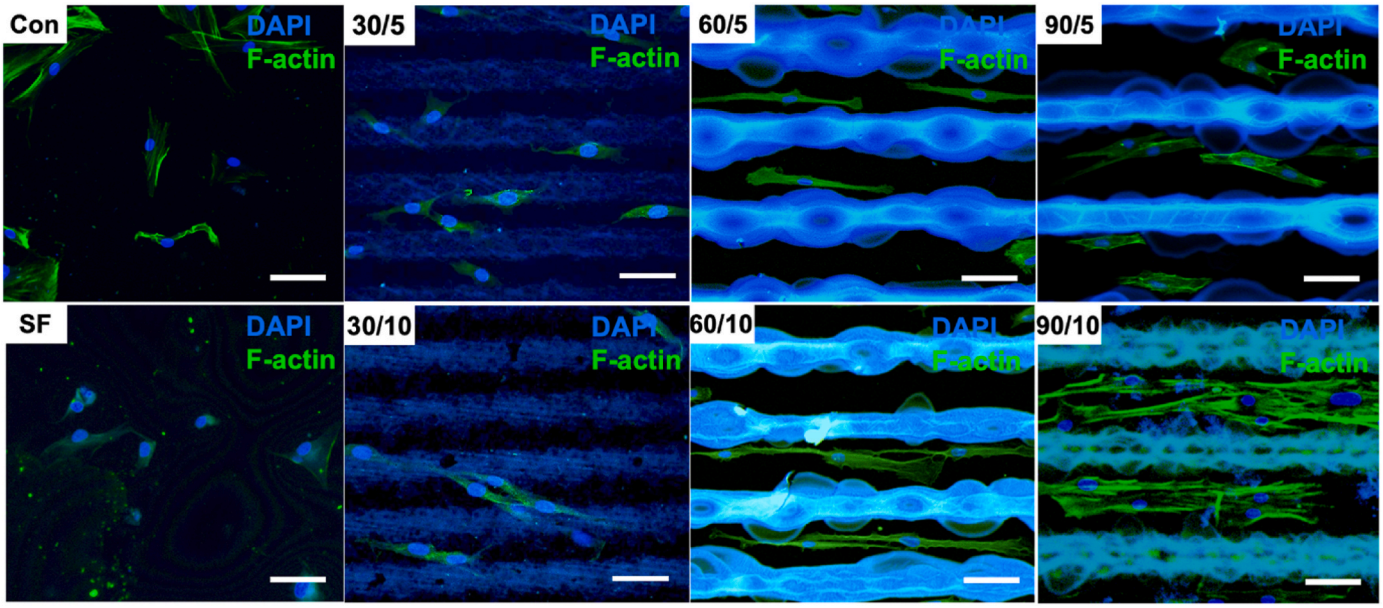

Fig. 5. The morphology of HGFs cultured on the zirconia surfaces with and without SFMG. The groups were marked as width/depth. Zirconia surface without SF was marked as the Control (Con) group, and Zirconia surface with SF uniformly sprayed coating was marked as the SF group. Representative fluorescence images of the morphology of HGFs cultured on the zirconia surfaces for 24 h. F-actin stained with FITC (green), and cell nuclei stained with DAPI (blue) (Scale bar = 50 μm). (For interpretation of the references to color in this figure legend, the reader is referred to the Web version of this article.)

3.5. SFMG promoted the adhesion, collagen expression, and migration of HGFs

The qRT-PCR and Western blot analyses demonstrated a notable increase in the expression of FN, COL1A1, and COL3A1 in the SFMG group compared to the control and SF groups (Fig. 7A a, b). These results suggested that the SFMG enhances both the adhesion capacity and collagen synthesis in HGFs.

Additionally, in the SFMG group, there was an upregulation in the expression of various chemokines and receptors in HGFs (Fig. 7B a). Results from the Transwell assay revealed an increased migration of HGFs to the bottom surface of the filter in the SFMG group, indicating that the supernatant from HGFs cultured in the SFMG group promotes cell migration (Fig. 7B b).

3.6. The effect of SFMG on HGFs was glycolytic-depended

The qRT-PCR data revealed a significant upregulation in the

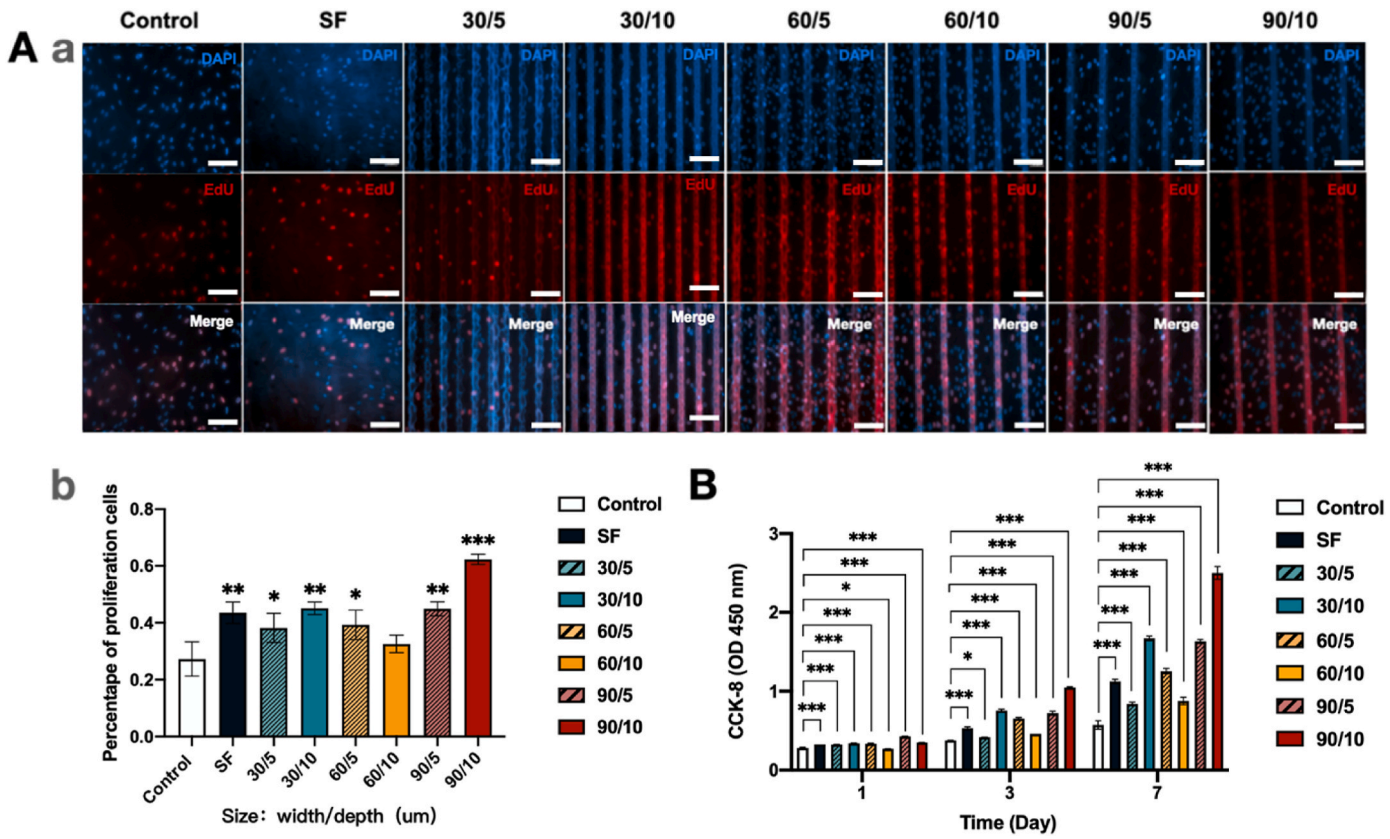

Fig. 6. The proliferation of HGFs cultured on the zirconia surfaces with and without SFMG. (A) (a) Representative images of EdU staining of HGFs cultured for 24 h. Nuclei stained with DAPI (blue) represented all cells, and nuclei stained with EdU (red) represented cells in the proliferation phase (Scale bar = 100 μm). (b) Percentages of cell proliferation in different groups (compared with the Control group: $*p < 0.05$, $**p < 0.01$, $***p < 0.001$). (B) Absorbance measurements for CCK-8 results of HGFs ($*p < 0.05$, $**p < 0.01$, $***p < 0.001$). (For interpretation of the references to color in this figure legend, the reader is referred to the Web version of this article.)

expression of key glycolytic enzymes in the HGFs of the SFMG group (Fig. 8A a). In terms of oxidative phosphorylation-related enzymes, only CS gene expression was elevated in the SFMG group (Fig. 8A b).

Inhibition of glycolysis in HGFs was observed to diminish the proliferative effects of the SFMG coatings, as indicated by the results of the EdU staining (Fig. 8B). Additionally, in the Transwell assay, the number of cells migrating through the filter pores significantly decreased in both the SF and SFMG groups after treatment with the glycolysis inhibitor 2-DG, and the differences between the three groups were nullified with the addition of 2-DG (Fig. 8C). Moreover, the expression of FN, COL1A1, and COL3A1 in HGFs was significantly reduced following the addition of 2-DG, as shown in both gene and protein expression analyses (Fig. 8D and E).

3.7. SFMG coatings regulated HGFs glycolysis function through the PI3K-AKT pathway

The Venn diagram depicted the intersecting DEGs among the comparative groups: Control vs. SF, SF vs. SFMG, and SFMG vs. Control (Fig. 9A). The hierarchical clustering heatmap demonstrated consistent gene expression patterns across the three replicate samples within each group (Fig. 9B a). This consistency was further evidenced by the observation that all co-expressed DEGs between the SF and SFMG groups followed similar expression trends, with certain DEGs exhibiting a sequential increase or decrease in line with the order from Control to SF to SFMG. RNA-sequencing results highlighted the most significant changes in DEGs associated with the PI3K-AKT pathway in the SFMG group (Fig. 9B b). Western blot analysis confirmed that the levels of PI3K, phosphorylated AKT, and phosphorylated mTOR were elevated in HGFs cultured on SFMG surfaces, indicating enhanced pathway activation (Fig. 9C and D).

Upon treatment with the PI3K inhibitor Ly294002, both the gene and protein expressions of PI3K were effectively suppressed (Fig. 9E and F). Additionally, the inhibition of PI3K led to a significant reduction in the expression of key glycolytic genes PGK1, LDHA, PKM2, and PFKFB3 in HGFs from the SFMG group, effectively eliminating the observed differences between the groups (Fig. 9G).

3.8. SFMG improved the soft tissue sealing around the zirconia abutment

Masson staining of tissue sections showed that in the SFMG group, collagen fibers surrounding the abutments were oriented vertically to the zirconia surface, in contrast to the other groups where the fibers did not exhibit a specific directional arrangement. Additionally, the SFMG group demonstrated the most extensive connective tissue integration, evidenced by the longest connective tissue length compared to the other groups (Fig. 10A a-c, B).

Immunofluorescence results indicated the highest fluorescence intensity for FN in the connective tissue around the abutments in the SFMG group, aligning with the *in vitro* findings (Fig. 10A d-f, C).

The HRP penetration assay, commonly used to evaluate the sealing capacity of soft tissues surrounding implants and abutments [41], showed that the HRP reaction was confined to the coronal area near the SFMG-modified surface. Conversely, in the control and SF groups, HRP penetration was observed deeper along the implant attachment, indicating a lesser sealing capability (Fig. 10A g-i, D).

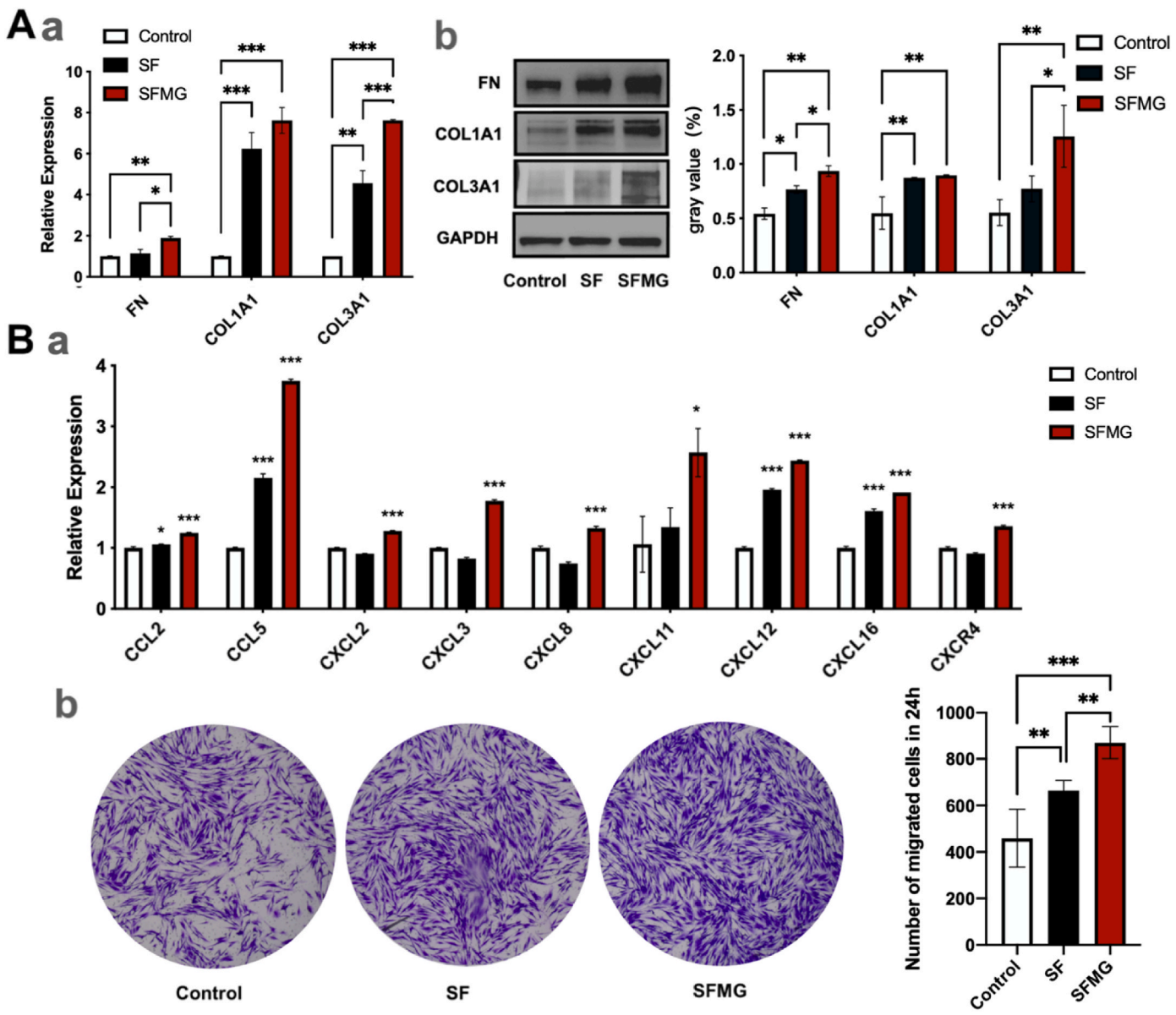

Fig. 7. Effects of 90/10 group (marked as SFMG) on the cell function of HGFs. (A) (a) The qRT-PCR results of FN, COL1A1 and COL3A1 in HGFs. (b) Representative western blot images and semi-quantitative statistical analysis of FN, COL1A1 and COL3A1 protein expression in HGFs. (B) (a) The qRT-PCR results of chemokine-related gene expression in HGFs cultured on specimens for 24 h. (b) Representative images (40 ×) and semi-quantitative statistical analysis of Transwell assay of HGFs. (*$p < 0.05$, **$p < 0.01$, ***$p < 0.001$).

4. Discussion

Compared to titanium abutments, zirconia had gained significant attention in recent years due to its superior aesthetic properties and favorable biocompatibility, making it an increasingly popular choice in implant dentistry. Since the importance of soft tissue sealing in preventing peri-implantitis was recognized, numerous attempts have been made to modify titanium abutment surfaces to enhance soft tissue integration. These include sandblasting [42], acid etching [43], plasma [40], and surface patterning modifications [44]. Among these modification methods, the introduction of microgroove morphology had been considered effective in inhibiting the apical migration of epithelial tissues. However, the mechanical processing methods suitable for titanium can severely damage the fatigue and flexural strength of zirconia [45,46]. Therefore, increasing soft tissue integration on zirconia abutments through surface modification is much more difficult than on titanium abutments.

Inkjet printing offers a solution, providing precise control over microscale surface morphology while maintaining the mechanical integrity of the base material. In our study, SFMG coatings with varying widths and depths were developed using inkjet printing with SF solution. Regarding the preparation process of SFMG, we need to emphasize one point. Before conducting the experiments, we chose to sterilize the samples using a high-temperature steam method. Some studies suggested that the high-temperature and high-pressure sterilization process can cause phase transformation in zirconia, thereby affecting its mechanical properties [47]. However, unlike high-temperature steam sterilization, these studies often expose zirconia materials to high temperature and pressure for longer periods, mostly over 5 h, and some even exceeding 200 h. In contrast, high-temperature steam sterilization procedures typically take less than 2 h. Studies that chose a treatment time within 2 h indicated that short-term high-temperature and high-pressure treatment resulted in an increase in the monoclinic phase in zirconia by less than 5 % [48,49]. Additionally, it has been shown that the flexural

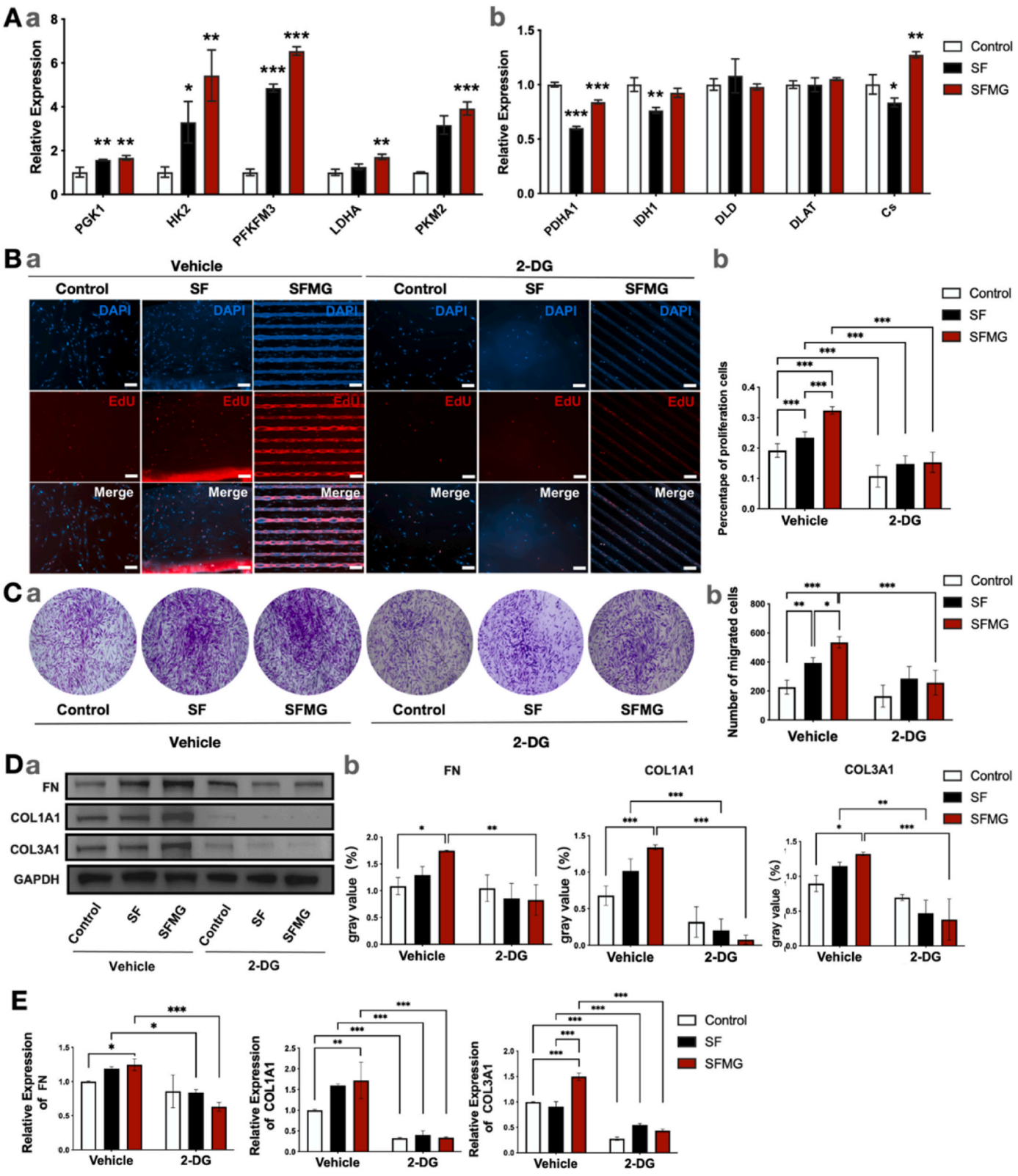

Fig. 8. The role of glucose metabolism in the effect of SFMG on HGFs. (A) The qRT-PCR results of gene expression of key enzymes of glycolysis (a) and oxidative phosphorylation (b) in HGFs cultured on specimens for 24 h. (B) Representative images of EdU staining (a) and percentages of cell proliferation (b) of HGFs cultured on the specimens for 24 h with or without glycolysis inhibitor 2-DG (Scale bar = 100 μm). (C) Representative images (a) and quantitative statistical analysis (b) of Transwell assay of HGFs cultured on specimens for 24 h with or without 2-DG. (D) Representative western blot images (a) and statistical analysis (b) of FN, COL1A1 and COL3A1 protein expression in HGFs cultured on specimens with or without 2-DG. (E) The qRT-PCR results of gene expression of FN, COL1A1 and COL3A1 in HGFs cultured on specimens with or without 2-DG (*$p < 0.05$, **$p < 0.01$, ***$p < 0.001$).

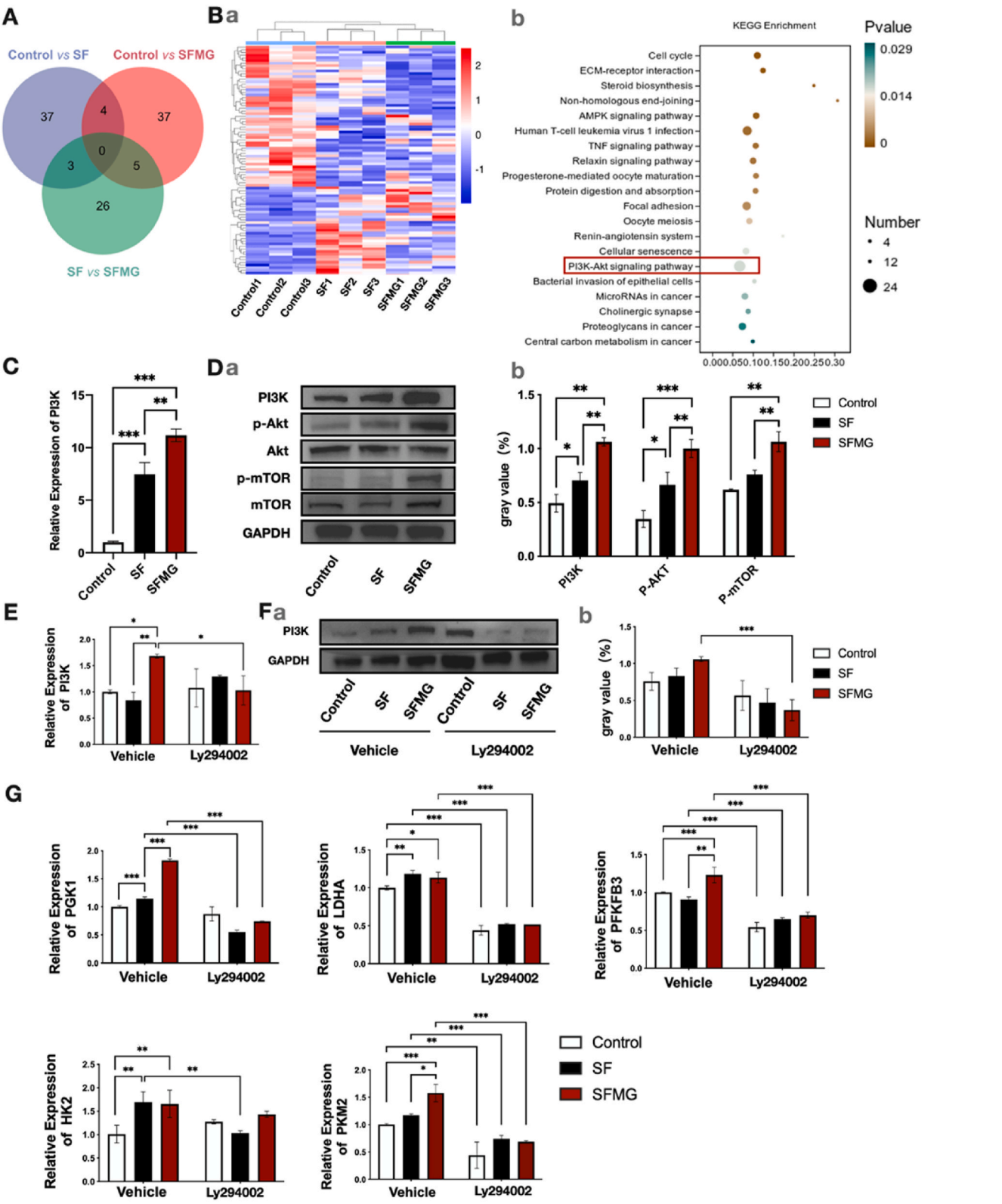

Fig. 9. SFMG activated PI3K-AKT pathway of HGFs. (A) Venn diagram of DEGs among the groups. (B) Bioinformation and function analysis of co-expressed DEGs among the groups. (a) Heatmap of co-expressed DEGs. (b) KEGG pathway enrichment analysis of co-expressed DEGs. (C) The qRT-PCR results of PI3K gene expression in HGFs cultured on specimens. (D) Representative western blot images (a) and quantitative statistical analysis (b) of the expression of proteins in the PI3K-AKT pathway in HGFs cultured on specimens. (E) The qRT-PCR results of PI3K gene expression in HGFs cultured on specimens with or without PI3K inhibitor Ly294002. (F) Representative western blot images (a) and quantitative statistical analysis (b) of PI3K protein expression in HGFs cultured on specimens with or without Ly294002. (G) The gene expression of key enzymes related to glycolysis in HGFs cultured on specimens with or without Ly294002 (*$p < 0.05$, **$p < 0.01$, ***$p < 0.001$).

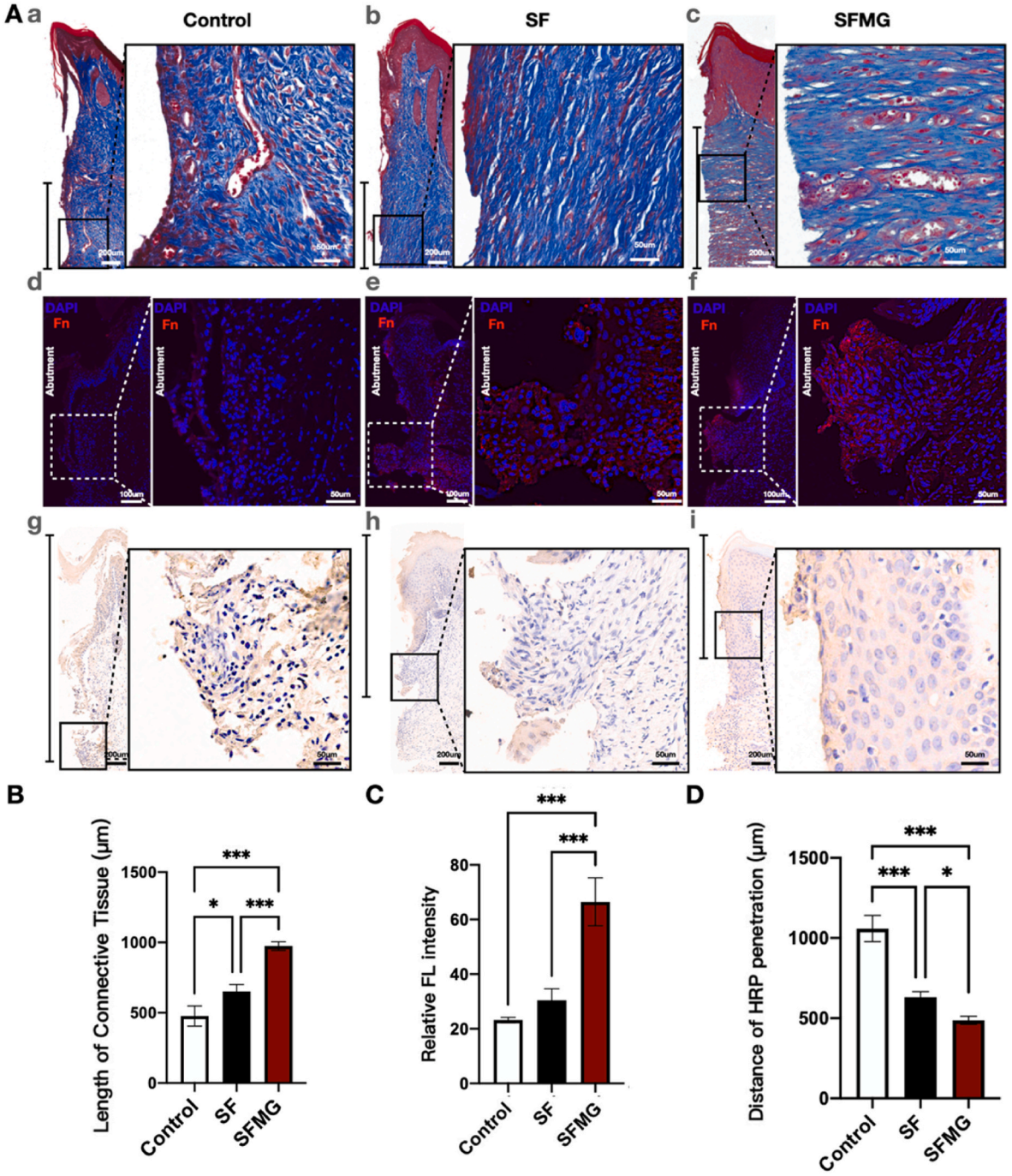

Fig. 10. Evaluation of the soft tissue integration properties of SFMG-coated zirconia abutment. (A) (a, b, c) Masson staining showed the length of connective tissue (the black ruler part) and the arrangement of collagen fibers in the connective tissue around the abutments (Scale bar = 200/50 μm). (d, e, f) Representative immunofluorescence images of FN (red) in the connective tissue around experimental abutments (Scale bar = 100/50 μm). (g, h, i) Typical path of HRP penetration (the black ruler part) around experimental implants and abutments (Scale bar = 200/50 μm). (B–D) Statistical analysis of the length of connective tissue (B), FN fluorescence (FL) intensity of connective tissue (C) and HRP penetration depth (D) around the abutments (*$p < 0.05$, **$p < 0.01$, ***$p < 0.001$). (For interpretation of the references to color in this figure legend, the reader is referred to the Web version of this article.)

strength of zirconia only significantly decreases when the monoclinic phase content exceeds 50 % [50]. However, we did not test the mechanical properties of zirconia before and after sterilization in this study, which is one of the limitations of our research. We found that SFMG in 60/5, 90/5, and 90/10 groups enhanced the hydrophilicity of the zirconia surface (Supplemental materials 2). This may because the raised SF ridges increased the contact area and surface energy of the ceramic surface. Studies have shown that compared with hydrophobic surfaces, hydrophilic surfaces have positive effects on the proliferation and adhesion of HGFs [51], while the optimal water contact angle for fibroblast growth on material surfaces is 50°–60° [51,52], which is consistent with the wettability of the 90/10 group. This may partially explain the most prominent cell proliferation-promoting ability displayed by the 90/10 group.

In addition to hydrophilicity, degradability is an important factor for the application of inkjet-printed SF coatings, and the degradation time should match the healing and regeneration of the surrounding soft tissues of the implant. The degradation performance of regenerated SF

biomaterials was closely related to the material form, extraction process, and treatment methods, with *in vivo* degradation time ranging from several months or even over a year [53]. In this study, we investigated the degradation of SFMG at 4 weeks *in vitro*, and although FTIR results showed some loss of components, microscopic observations revealed that the grooved morphology was still intact. This might be related to the degradation characteristics of SF, which degraded in a surface erosion mode, gradually losing components from the surface to the center, meaning its morphological structure could remain intact for a long time during the degradation process, without sudden collapse [54]. This is undoubtedly beneficial for the stability of the soft tissues around the implant, as study had shown that the presence of grooved structures could enhance the anchoring function of connective tissue and slow the movement of epithelium towards the root [20].

The integration between the SFMG coating and the abutment should be able to withstand various external forces that may be encountered during clinical applications. These forces may arise from several operational processes, including sterilization procedures before clinical use, routine cleaning during use, and micromovements due to masticatory forces during functional loading. To evaluate the adhesion strength of the SFMG coatings on zirconia, we conducted tape peel tests according to the ASTM D3359 standard. The results indicated that the coatings achieved a 4B rating, demonstrating high adhesion strength (Supplemental materials 3). In our opinion, this adhesion strength primarily originated from several factors. Firstly, mechanical interlocking. It has been found that changes in the surface roughness of materials could affect the adhesion of SF coatings [55], indicating that physical adhesion plays a role in the bonding of SF coatings to materials. Additionally, the piezoelectric inkjet printing process could enhance the adhesion of SF. Yucel et al. [56] found that applying a DC voltage to SF solutions disrupted the charge balance of the solution, causing SF molecules to aggregate into nanoparticles and microspheres, thereby increasing the adhesion of the coatings. But we must acknowledge that the testing of the coating's adhesion to the abutment in this study was limited to *in vitro* simulations, which cannot fully reflect the actual conditions in clinical applications. The stability of the coating in a clinical environment remains to be further investigated.

When cells interact with a non-uniform substrate featuring variations in height, they often grow in a highly polarized manner along the contours of these elevated structures, a phenomenon referred to as "contact guidance" [57]. In this study, SFMG coatings demonstrated differing levels of contact guidance based on their depth and width. Specifically, HGFs exhibited a trend of directional alignment within microgrooves measuring 60 μm and 90 μm in width, predominantly positioning themselves at the bottom of these grooves with their long axes parallel to the grooves. There may be two reasons for this phenomenon. On the one hand, gravity and the height of the SF ridge limited the vertical movement of cells, and the narrow width of the SF ridge was not conducive to the expansion of cells, thus causing more cells to be deposited at the bottom of the groove rather than surface of SF ridges. On the other hand, the phenomenon of cell contact guidance is intricately linked to the adhesion dynamics between cells and the substrate [15]. FN, a vital extracellular matrix molecule, plays a key role in the formation of focal adhesions between cells and the extracellular matrix [58]. It has been observed that FN tends to accumulate at the edges of grooved topographies [59], providing an initial cue for cell adhesion [60]. This directional adhesion, facilitated through the formation of focal adhesions, leads to the polarized arrangement of HGFs. The alignment direction of HGFs is a critical factor influencing the integration of peri-implant connective tissue [61]. In line with previous findings, our results also indicated an increase in collagen fibers oriented vertically to the abutment surface, in contrast to the disorganized arrangement seen in control groups. This observation led us to investigate how the circular arrangement of HGFs along the abutment surface could cause collagen fibers to align perpendicularly. We hypothesize that HGFs might secrete chemokines to attract more distant HGFs. During their migration, HGFs could also express and secrete collagen fibers, leading to a macroscopic alignment perpendicular to the abutment surface. This study confirmed an increase in chemokine and collagen expression in HGFs, as well as enhanced HGF migration.

The polarized alignment of HGFs was correlated with enhanced cell proliferation, notably within the 90/10 group. This finding differed from Kim et al.'s study, which concluded that grooves with a width of 60 μm and a depth of 10 μm on titanium surfaces most effectively promoted proliferation of fibroblasts. The discrepancy was likely due to the different materials used, as research had shown that aside from the size of the microgrooves, their hardness and tension could also affect cell growth [62]. Interestingly, the increase in proliferation was not exclusive to groups with microgroove dimensions of 60 μm and 90 μm, but was also evident in the SF, 30/5, and 30/10 groups in our study. This trend could be attributed to the effects of SF, which has been previously demonstrated to promote the proliferation and migration of HGFs, thereby aiding in soft tissue repair and healing processes [32,63]. Regarding the mechanism by which SF exerts its bioactive effects, current researchers have different theories. Some researchers believed that the ability of SF to promote cell proliferation is related to its RGD (arginine-glycine-aspartic acid) sequence, which can enhance cell attachment [64]. More recent studies have further elucidated the possible molecular mechanisms underlying the bioactive effects of SF. The study by Ye Ri Park et al. [32] suggested that SF promoted fibroblast proliferation and migration by activating the NF-κB pathway and its downstream molecules in fibroblasts. On the other hand, the study by Celia Martínez-Mora et al. suggested that the bioactivity of SF was highly related to the activation of c-JNK (c-Jun N-terminal kinase) and PI3K in cells [65]. This discrepancy may be due to the different sources of fibroblasts used in the studies. In our study, we also observed the activation of the PI3K pathway and its downstream signaling in HGFs.

Cellular activities, particularly during proliferation, demand an ample energy supply, primarily sourced from glucose catabolism encompassing both oxidative phosphorylation and glycolysis. It has been reported that normal tissue cells often experience increased rates of glycolysis during proliferation phases [66]. According to Matthew et al. [67], glycolysis provides a rapid source of energy and produces essential precursors for cell proliferation, such as acetyl-coenzyme A and reduced coenzyme II. The inhibition of critical glycolytic enzymes, like LDHA, markedly impacts cell proliferation [68]. Our findings align with this concept, showing an upregulation in the expression of glycolysis-associated enzymes in HGFs of the SFMG group. Furthermore, the stimulatory effect of SFMG on HGF proliferation was negated upon glycolysis inhibition. This is consistent with findings from Pamela et al. [57], who observed similar trends in the context of skin wound healing.

We delved into the intracellular mechanisms through which the groove morphology influences the glucose metabolism of HGFs. Cells respond to the complex structures and local topography of the ECM by adapting their shape, movement, and lifecycle, a phenomenon referred to as mechanotransduction [69]. In our study, RNA-sequencing analysis highlighted a significant enrichment of DEGs associated with focal adhesion kinase (FAK) and the PI3K-AKT pathway in HGFs, comparing the SFMG and control groups. The PI3K-AKT pathway, known to be crucial for transducing extracellular mechanical signals, operates downstream of FAK which is closely linked to cell adhesion and morphological changes. This pathway can be activated by integrins during cell-ECM interaction, playing a vital role in regulating cell proliferation and migration [70,71]. Furthermore, the PI3K-AKT pathway acts as a bridge between mechanical signals and cellular metabolism [72]. AKT, a downstream effector of PI3K, can boost glycolysis by suppressing the forkhead box O (FOXO) transcription factors, curtailing glycolytic branch reactions, and directly enhancing the activity of key glycolytic enzymes such as HK2 [73]. Our results confirmed the activation of the PI3K-AKT-mTOR pathway in HGFs in the SFMG group. Upon inhibiting PI3K, the stimulatory effect of the SFMG on the expression of key glycolytic enzymes in HGFs was abolished.

Despite discovering some interesting phenomena in this study, there are still some limitations due to various constraints. One limitation of this study is the relatively short duration of the *in vitro* and *in vivo* experiments. While the results are promising, longer-term studies are necessary to fully understand the durability and stability of the SFMG coatings in a clinical setting. Besides, the study focused on a specific type of cell (HGFs). However, other cells such as macrophages and vascular endothelial cells also play important roles in soft tissue integration [74]. Therefore, in future studies, we aim to involve longer-term *in vivo* research. These studies should monitor the degradation behavior, mechanical stability, and tissue response over time, as well as the interactions between various cell types on the surface of SFMG coatings.

5. Conclusion

We developed SFMG coatings with stable chemical and physical characteristics on zirconia ceramic surfaces, determining that the optimal microgroove dimensions were 90 μm in width and 10 μm in depth. The SFMG-coated zirconia surfaces enhanced the proliferation, adhesion, collagen synthesis, and migration capabilities of HGFs, and improved soft tissue sealing around the abutments. The beneficial effects of SFMG on HGFs were found to be glycolysis-dependent and mediated through the PI3K-AKT-mTOR pathway. This study lays a theoretical foundation for reducing the occurrence of peri-implantitis and enhancing the success rates of dental implant restorations.

CRediT authorship contribution statement

Yinuo Yan: Visualization, Investigation. **Qiqian Yan:** Visualization, Investigation. **Kexin Cai:** Writing – original draft, Data curation. **Zhihan Wang:** Validation, Software. **Qiulan Li:** Validation, Software. **Ke Zhao:** Methodology. **Yutao Jian:** Methodology. **Xiaoshi Jia:** Writing – review & editing, Supervision, Conceptualization.

Declaration of competing interest

The authors declare that they have no known competing financial interests or personal relationships that could have appeared to influence the work reported in this paper.

Data availability

Data will be made available on request.

Acknowledgments

This work was supported by funds from the National Key Research and Development Program of China (grant number 2022YFC2410104), from the National Natural Science Foundation of China (82071156 to K. Z.) and by the Science and Technology Projects in Guangzhou (202201010992 to X.J.).

Appendix A. Supplementary data

Supplementary data to this article can be found online at https://doi.org/10.1016/j.mtbio.2024.101158.

References

[1] H.S. Alghamdi, J.A. Jansen, The development and future of dental implants, Dent. Mater. J. 39 (2020) 167–172, https://doi.org/10.4012/dmj.2019-140.
[2] S. Barootchi, H.L. Wang, Peri-implant diseases: current understanding and management, Int. J. Oral Implant. 14 (2021) 263–282. https://www.ncbi.nlm.nih.gov/pubmed/34415128.
[3] F. Schwarz, A. Ramanauskaite, It is all about peri-implant tissue health, Periodontol 88 (2000) 9–12, https://doi.org/10.1111/prd.12407, 2022.
[4] S. Jepsen, J.G. Caton, J.M. Albandar, N.F. Bissada, P. Bouchard, P. Cortellini, K. Demirel, M. de Sanctis, C. Ercoli, J. Fan, N.C. Geurs, F.J. Hughes, L. Jin, A. Kantarci, E. Lalla, P.N. Madianos, D. Matthews, M.K. McGuire, M.P. Mills, P. M. Preshaw, M.A. Reynolds, A. Sculean, C. Susin, N.X. West, K. Yamazaki, Periodontal manifestations of systemic diseases and developmental and acquired conditions: consensus report of workgroup 3 of the 2017 world workshop on the classification of periodontal and peri-implant diseases and conditions, J. Periodontol. 89 (Suppl 1) (2018) S237–S248, https://doi.org/10.1002/JPER.17-0733.
[5] A. Stavropoulos, K. Bertl, L. Winning, I. Polyzois, What is the influence of implant surface characteristics and/or implant material on the incidence and progression of peri-implantitis? A systematic literature review, Clin. Oral Implants Res. 32 (Suppl 21) (2021) 203–229, https://doi.org/10.1111/clr.13859.
[6] R. Cosgarea, A. Sculean, J.A. Shibli, G.E. Salvi, Prevalence of peri-implant diseases - a critical review on the current evidence, Braz. Oral Res. 33 (Suppl 1) (2019) e063, https://doi.org/10.1590/1807-3107bor-2019.vol33.0063.
[7] F. Schwarz, J. Derks, A. Monje, H.L. Wang, Peri-implantitis, J. Periodontol. 89 (Suppl 1) (2018) S267–S290, https://doi.org/10.1002/JPER.16-0350.
[8] S. Ivanovski, R. Lee, Comparison of peri-implant and periodontal marginal soft tissues in health and disease, Periodontol 76 (1) (2000. 2018) 116–130, https://doi.org/10.1111/prd.12150.
[9] Z. Zheng, X. Ao, P. Xie, F. Jiang, W. Chen, The biological width around implant, J Prosthodont Res 65 (1) (2021) 11–18, https://doi.org/10.2186/jpr.JPOR_2019_356.
[10] Y. Zhang, B.R. Lawn, Evaluating dental zirconia, Dent. Mater. 35 (2019) 15–23, https://doi.org/10.1016/j.dental.2018.08.291.
[11] K. Tang, M. Luo, W. Zhou, L. Niu, J. Chen, F. Wang, The integration of peri-implant soft tissues around zirconia abutments: challenges and strategies, Bioact. Mater. 27 (2023) 348–361, https://doi.org/10.1016/j.bioactmat.2023.04.009.
[12] N. Enkling, M. Marder, S. Bayer, W. Götz, M. Stoilov, D. Kraus, Soft tissue response to different abutment materials: a controlled and randomized human study using an experimental model, Clin. Oral Implants Res. 33 (6) (2022) 667–679, https://doi.org/10.1111/clr.13932.
[13] S.J. Paul, D. Nesic, Influence of the transmucosal surface of dental implants on the soft tissue attachment level and marginal bone loss in preclinical studies: a systematic review, Int. J. Oral Maxillofac. Implants 39 (2024) 173–183, https://doi.org/10.11607/jomi.10398.
[14] T. Hanawa, Zirconia versus titanium in dentistry: a review, Dent. Mater. J. 39 (2020) 24–36, https://doi.org/10.4012/dmj.2019-172.
[15] C. Leclech, C. Villard, Cellular and subcellular contact guidance on microfabricated substrates, Front. Bioeng. Biotechnol. 8 (2020) 551505, https://doi.org/10.3389/fbioe.2020.551505.
[16] C. Leclech, A.I. Barakat, Is there a universal mechanism of cell alignment in response to substrate topography? Cytoskeleton (Hoboken) 78 (2021) 284–292, https://doi.org/10.1002/cm.21661.
[17] S. Paul, O. Hanisch, D. Nesic, Human gingival fibroblast proliferation on materials used for dental implant abutments: a systematic review, Int. J. Prosthodont. (IJP) 34 (2021) 811–828, https://doi.org/10.11607/ijp.7388.
[18] E. Corvino, P. Pesce, R. Mura, E. Marcano, L. Canullo, Influence of modified titanium abutment Surface on peri-implant soft tissue behavior: a systematic review of *in vitro* studies, Int. J. Oral Maxillofac. Implants 35 (2020) 503–519, https://doi.org/10.11607/jomi.8110.
[19] R.R. Martins de Barros, M.M. Provinciatti, V.A. Muglia, A.B. Novaes Jr., The effect of laser-lok abutments on fiber orientation and buccal bone remodeling: a histomorphometric study, Int. J. Periodontics Restor. Dent. 40 (2020) 73–81, https://doi.org/10.11607/prd.4426.
[20] G. Iglhaut, F. Schwarz, R.R. Winter, I. Mihatovic, M. Stimmelmayr, H. Schliephake, Epithelial attachment and downgrowth on dental implant abutments–a comprehensive review, J. Esthetic Restor. Dent. 26 (2014) 324–331, https://doi.org/10.1111/jerd.12097.
[21] E. Roitero, M. Anglada, F. Mucklich, E. Jimenez-Pique, Mechanical reliability of dental grade zirconia after laser patterning, J. Mech. Behav. Biomed. Mater. 86 (2018) 257–263, https://doi.org/10.1016/j.jmbbm.2018.06.039.
[22] N. Scoutaris, S. Ross, D. Douroumis, Current trends on medical and pharmaceutical applications of inkjet printing technology, Pharm. Res. (N. Y.) 33 (2016) 1799–1816, https://doi.org/10.1007/s11095-016-1931-3.
[23] X. Li, B. Liu, B. Pei, J. Chen, D. Zhou, J. Peng, X. Zhang, W. Jia, T. Xu, Inkjet bioprinting of biomaterials, Chem. Rev. 120 (2020) 10793–10833, https://doi.org/10.1021/acs.chemrev.0c00008.
[24] X. Jian, W. Huang, D. Wu, D. You, Z. Lin, J. Chen, Effect of fibronectin-coated micro-grooved titanium surface on alignment, adhesion, and proliferation of human gingival fibroblasts, Med. Sci. Mon. Int. Med. J. Exp. Clin. Res. 23 (2017) 4749–4759, https://doi.org/10.12659/msm.903883.
[25] C.E. Van den Borre, B.G.R. Zigterman, M.Y. Mommaerts, A. Braem, How surface coatings on titanium implants affect keratinized tissue: a systematic review, J. Biomed. Mater. Res. B Appl. Biomater. 110 (7) (2022) 1713–1723, https://doi.org/10.1002/jbm.b.35025.
[26] D. Ito, T. Kado, F. Nagano-Takebe, T. Hidaka, K. Endo, Y. Furuichi, Biological activation of zirconia surfaces by chemical modification with IGF-1, J. Biomed. Mater. Res. 103 (2015) 3659–3665, https://doi.org/10.1002/jbm.a.35476.
[27] Y. Wang, Y. Zhang, D. Jing, Y. Shuang, R.J. Miron, Enamel matrix derivative improves gingival fibroblast cell behavior cultured on titanium surfaces, Clin. Oral Invest. 20 (2016) 685–695, https://doi.org/10.1007/s00784-015-1558-5.
[28] A. Vilaca, R.M.A. Domingues, H. Tiainen, B.B. Mendes, A. Barrantes, R.L. Reis, M. E. Gomes, M. Gomez-Florit, Multifunctional surfaces for improving soft tissue integration, Adv. Healthcare Mater. 10 (2021) e2001985, https://doi.org/10.1002/adhm.202001985.

[29] X. Ding, X. Wei, Y. Huang, C. Guan, T. Zou, S. Wang, H. Liu, Y. Fan, Delivery of demineralized bone matrix powder using a salt-leached silk fibroin carrier for bone regeneration, J. Mater. Chem. B 3 (2015) 3177–3188, https://doi.org/10.1039/c5tb00046g.
[30] M. Gholipourmalekabadi, S. Sapru, A. Samadikuchaksaraei, R.L. Reis, D.L. Kaplan, S.C. Kundu, Silk fibroin for skin injury repair: where do things stand? Adv. Drug Deliv. Rev. 153 (2020) 28–53, https://doi.org/10.1016/j.addr.2019.09.003.
[31] Y. Zhang, Y. Jian, X. Jiang, X. Li, X. Wu, J. Zhong, X. Jia, Q. Li, X. Wang, K. Zhao, Y. Yao, Stepwise degradable PGA-SF core-shell electrospinning scaffold with superior tenacity in wetting regime for promoting bone regeneration, Mater Today Bio 26 (2024) 101023, https://doi.org/10.1016/j.mtbio.2024.101023.
[32] Y.R. Park, M.T. Sultan, H.J. Park, J.M. Lee, H.W. Ju, O.J. Lee, D.J. Lee, D.L. Kaplan, C.H. Park, NF-kappaB signaling is key in the wound healing processes of silk fibroin, Acta Biomater. 67 (2018) 183–195, https://doi.org/10.1016/j.actbio.2017.12.006.
[33] H. Tao, B. Marelli, M. Yang, B. An, M.S. Onses, J.A. Rogers, D.L. Kaplan, F. G. Omenetto, Inkjet printing of regenerated silk fibroin: from printable forms to printable functions, Adv. Mater. 27 (2015) 4273–4279, https://doi.org/10.1002/adma.201501425.
[34] R.J. DeBerardinis, C.B. Thompson, Cellular metabolism and disease: what do metabolic outliers teach us? Cell 148 (2012) 1132–1144, https://doi.org/10.1016/j.cell.2012.02.032.
[35] J. Zhu, C.B. Thompson, Metabolic regulation of cell growth and proliferation, Nat. Rev. Mol. Cell Biol. 20 (2019) 436–450, https://doi.org/10.1038/s41580-019-0123-5.
[36] T. Isogai, J.S. Park, G. Danuser, Cell forces meet cell metabolism, Nat. Cell Biol. 19 (2017) 591–593, https://doi.org/10.1038/ncb3542.
[37] M. Ball, D.M. Grant, W.J. Lo, C.A. Scotchford, The effect of different surface morphology and roughness on osteoblast-like cells, J. Biomed. Mater. Res. 86 (2008) 637–647, https://doi.org/10.1002/jbm.a.31652.
[38] T.M.J. Evers, L.J. Holt, S. Alberti, A. Mashaghi, Publisher correction: reciprocal regulation of cellular mechanics and metabolism, Nat. Metab. 3 (2021) 876–877, https://doi.org/10.1038/s42255-021-00423-6.
[39] T. Guo, K. Gulati, H. Arora, P. Han, B. Fournier, S. Ivanovski, Race to invade: understanding soft tissue integration at the transmucosal region of titanium dental implants, Dent. Mater. 37 (2021) 816–831, https://doi.org/10.1016/j.dental.2021.02.005.
[40] P. Pesce, M. Menini, G. Santori, E. Giovanni, F. Bagnasco, L. Canullo, Photo and plasma activation of dental implant titanium surfaces. A systematic review with meta-analysis of pre-clinical studies, J. Clin. Med. 9 (2020) 2817, https://doi.org/10.3390/jcm9092817.
[41] I. Narimatsu, I. Atsuta, Y. Ayukawa, W. Oshiro, N. Yasunami, A. Furuhashi, K. Koyano, Epithelial and connective tissue sealing around titanium implants with various typical surface finishes, ACS Biomater. Sci. Eng. 5 (2019) 4976–4984, https://doi.org/10.1021/acsbiomaterials.9b00499.
[42] F.P. Nothdurft, D. Fontana, S. Ruppenthal, A. May, C. Aktas, Y. Mehraein, P. Lipp, L. Kaestner, Differential behavior of fibroblasts and epithelial cells on structured implant abutment materials: a comparison of materials and surface topographies, Clin. Implant Dent. Relat. Res. 17 (2015) 1237–1249, https://doi.org/10.1111/cid.12253.
[43] P. Pesce, M. Menini, G. Tommasato, R. Patini, L. Canullo, Influence of modified titanium abutment surface on peri-implant soft tissue behaviour: a systematic review of histological findings, Int. J. Oral Implant. 12 (4) (2019) 419–429.
[44] D. Baltriukiene, V. Sabaliauskas, E. Balciunas, A. Melninkaitis, E. Liutkevicius, V. Bukelskiene, V. Rutkunas, The effect of laser-treated titanium surface on human gingival fibroblast behavior, J. Biomed. Mater. Res. 102 (2014) 713–720, https://doi.org/10.1002/jbm.a.34739.
[45] W. Li, Q. Ding, F. Sun, B. Liu, F. Yuan, L. Zhang, R. Bao, J. Gu, Y. Lin, Fatigue behavior of zirconia with microgrooved surfaces produced using femtosecond laser, Laser Med. Sci. 38 (2023) 33, https://doi.org/10.1007/s10103-022-03679-w.
[46] W.J. Li, Q. Ding, F.S. Yuan, F.B. Sun, J.Q. Zheng, R. Bao, L. Zhang, Effects of femtosecond laser treatment on surface characteristics and flexural strength of zirconia, Beijing Da Xue Xue Bao Yi Xue Ban 53 (2021) 770–775, https://doi.org/10.19723/j.issn.1671-167X.2021.04.025.
[47] H. Yang, Y.L. Xu, G. Hong, H. Yu, Effects of low-temperature degradation on the surface roughness of yttria-stabilized tetragonal zirconia polycrystal ceramics: a systematic review and meta-analysis, J. Prosthet. Dent 125 (2) (2021) 222–230, https://doi.org/10.1016/j.prosdent.2020.01.005.
[48] T.J. Lucas, N.C. Lawson, G.M. Janowski, J.O. Burgess, Phase transformation of dental zirconia following artificial aging, J. Biomed. Mater. Res. B Appl. Biomater. 103 (7) (2015) 1519–1523, https://doi.org/10.1002/jbm.b.33334.
[49] G.K.R. Pereira, A.B. Venturini, T. Silvestri, K.S. Dapieve, A.F. Montagner, F.Z. M. Soares, L.F. Valandro, Low-temperature degradation of Y-TZP ceramics: a systematic review and meta-analysis, J. Mech. Behav. Biomed. Mater. 55 (2015 Mar) 151–163, https://doi.org/10.1016/j.jmbbm.2015.10.017.
[50] H.T. Kim, J.S. Han, J.H. Yang, J.B. Lee, S.H. Kim, The effect of low temperature aging on the mechanical property & phase stability of Y-TZP ceramics, J Adv Prosthodont 1 (3) (2009) 113–117, https://doi.org/10.4047/jap.2009.1.3.113.
[51] Y.S. Kim, S.Y. Shin, S.K. Moon, S.M. Yang, Surface properties correlated with the human gingival fibroblasts attachment on various materials for implant abutments: a multiple regression analysis, Acta Odontol. Scand. 73 (2015) 38–47, https://doi.org/10.3109/00016357.2014.949845.
[52] A.S. Rozeik, M.S. Chaar, S. Sindt, S. Wille, C. Selhuber-Unkel, M. Kern, S. El-Kholy, C. Dorfer, K.M. Fawzy El-Sayed, Cellular properties of human gingival fibroblasts on novel and conventional implant-abutment materials, Dent. Mater. 38 (2022) 540–548, https://doi.org/10.1016/j.dental.2021.12.139.
[53] O.J. Lee, J.M. Lee, J.H. Kim, J. Kim, H. Kweon, Y.Y. Jo, C.H. Park, Biodegradation behavior of silk fibroin membranes in repairing tympanic membrane perforations, J. Biomed. Mater. Res. 100 (2012) 2018–2026, https://doi.org/10.1002/jbm.a.33308.
[54] D. Badillo-Sanchez, D. Chelazzi, R. Giorgi, A. Cincinelli, P. Baglioni, Characterization of the secondary structure of degummed Bombyx mori silk in modern and historical samples, Polym. Degrad. Stabil. 57 (2018) 53–62, https://doi.org/10.1016/j.polymdegradstab.2018.09.022.
[55] R. Elia, C.D. Michelson, A.L. Perera, T.F. Brunner, M. Harsono, G.G. Leisk, G. Kugel, D.L. Kaplan, Electrodeposited silk coatings for bone implants, J. Biomed. Mater. Res. B Appl. Biomater. 103 (2015) 1602–1609, https://doi.org/10.1002/jbm.b.33351.
[56] T. Yucel, N. Kojic, G.G. Leisk, T.J. Lo, D.L. Kaplan, Non-equilibrium silk fibroin adhesives, J. Struct. Biol. 170 (2010) 406–412, https://doi.org/10.1016/j.jsb.2009.12.012.
[57] X. Zhao, P. Psarianos, L.S. Ghoraie, K. Yip, D. Goldstein, R. Gilbert, I. Witterick, H. Pang, A. Hussain, J.H. Lee, J. Williams, S.V. Bratman, L. Ailles, B. Haibe-Kains, F.F. Liu, Metabolic regulation of dermal fibroblasts contributes to skin extracellular matrix homeostasis and fibrosis, Nat. Metab. 1 (2019) 147–157, https://doi.org/10.1038/s42255-018-0008-5.
[58] J. Patten, K. Wang, Fibronectin in development and wound healing, Adv. Drug Deliv. Rev. 170 (2021) 353–368, https://doi.org/10.1016/j.addr.2020.09.005.
[59] A. Weidt, S.G. Mayr, M. Zink, Influence of topological cues on fibronectin adsorption and contact guidance of fibroblasts on microgrooved titanium, ACS Appl. Bio Mater. 2 (2019) 1066–1077, https://doi.org/10.1021/acsabm.8b00667.
[60] C.J. Dalton, C.A. Lemmon, Fibronectin: molecular structure, fibrillar structure and mechanochemical signaling, Cells 10 (9) (2021) 2443, https://doi.org/10.3390/cells10092443.
[61] Y. Lai, J. Chen, T. Zhang, D. Gu, C. Zhang, Z. Li, S. Lin, X. Fu, S. Schultze-Mosgau, Effect of 3D microgroove surface topography on plasma and cellular fibronectin of human gingival fibroblasts, J. Dent. 41 (2013) 1109–1121, https://doi.org/10.1016/j.jdent.2013.08.004.
[62] A. Saraswathibhatla, D. Indana, O. Chaudhuri, Cell-extracellular matrix mechanotransduction in 3D, Nat. Rev. Mol. Cell Biol. 24 (7) (2023) 495–516, https://doi.org/10.1038/s41580-023-00583-1.
[63] W. Zhang, L. Chen, J. Chen, L. Wang, X. Gui, J. Ran, G. Xu, H. Zhao, M. Zeng, J. Ji, L. Qian, J. Zhou, H. Ouyang, X. Zou, Silk fibroin biomaterial shows safe and effective wound healing in animal models and a randomized controlled clinical trial, Adv. Healthcare Mater. 6 (10) (2017) 1700121, https://doi.org/10.1002/adhm.201700121.
[64] J.H. Cherng, S.J. Chang, Y.K. Chiu, Y.H. Chiu, T.J. Fang, H.C. Chen, Low molecular weight sericin enhances the in vitro of immunological modulation and cell migration, Front. Bioeng. Biotechnol. 10 (2022) 925197, https://doi.org/10.3389/fbioe.2022.925197.
[65] C. Martinez-Mora, A. Mrowiec, E.M. Garcia-Vizcaino, A. Alcaraz, J.L. Cenis, F. J. Nicolas, Fibroin and sericin from Bombyx mori silk stimulate cell migration through upregulation and phosphorylation of c-Jun, PLoS One 7 (2012) e42271, https://doi.org/10.1371/journal.pone.0042271.
[66] K. Schroder, NADPH oxidases in redox regulation of cell adhesion and migration, Antioxidants Redox Signal. 20 (2014) 2043–2058, https://doi.org/10.1089/ars.2013.5633.
[67] Heiden M.G. Vander, L.C. Cantley, C.B. Thompson, Understanding the Warburg effect: the metabolic requirements of cell proliferation, Science 324 (2009) 1029–1033, https://doi.org/10.1126/science.1160809.
[68] D. Sharma, M. Singh, R. Rani, Role of LDH in tumor glycolysis: regulation of LDHA by small molecules for cancer therapeutics, Semin. Cancer Biol. 87 (2022) 184–195, https://doi.org/10.1016/j.semcancer.2022.11.007.
[69] A. Saraswathibhatla, D. Indana, O. Chaudhuri, Cell-extracellular matrix mechanotransduction in 3D, Nat. Rev. Mol. Cell Biol. 24 (2023) 495–516, https://doi.org/10.1038/s41580-023-00583-1.
[70] P. Tiemin, M. Fanzheng, X. Peng, H. Jihua, S. Ruipeng, L. Yaliang, W. Yan, X. Junlin, L. Qingfu, H. Zhefeng, L. Jian, G. Zihao, L. Guoxing, S. Boshi, Z. Ming, M. Qinghui, L. Desen, L. Lianxin, MUC13 promotes intrahepatic cholangiocarcinoma progression via EGFR/PI3K/AKT pathways, J. Hepatol. 72 (2020) 761–773, https://doi.org/10.1016/j.jhep.2019.11.021.
[71] N. Borreguero-Munoz, G.C. Fletcher, M. Aguilar-Aragon, A. Elbediwy, Z.I. Vincent-Mistiaen, B.J. Thompson, The Hippo pathway integrates PI3K-Akt signals with mechanical and polarity cues to control tissue growth, PLoS Biol. 17 (2019) e3000509, https://doi.org/10.1371/journal.pbio.3000509.
[72] M. Di-Luoffo, Z. Ben-Meriem, P. Lefebvre, M. Delarue, J. Guillermet-Guibert, PI3K functions as a hub in mechanotransduction, Trends Biochem. Sci. 46 (2021) 878–888, https://doi.org/10.1016/j.tibs.2021.05.005.
[73] J.P. Shiau, Y.T. Chuang, Y.B. Cheng, J.Y. Tang, M.F. Hou, C.Y. Yen, H.W. Chang, Impacts of Oxidative Stress and PI3K/AKT/mTOR on Metabolism and the future direction of investigating fucoidan-modulated metabolism, Antioxidants 11 (2022) 911, https://doi.org/10.3390/antiox11050911.
[74] M. Baseri, F. Radmand, R. Hamedi, M. Yousefi, H.S. Kafil, Immunological aspects of dental implant rejection, BioMed Res. Int. 2020 (2020) 7279509, https://doi.org/10.1155/2020/7279509.